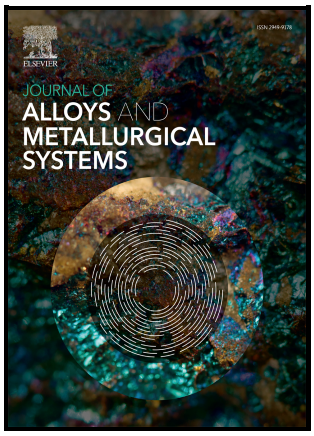

Design of lightweight high temperature structural materials based on Ti–Mo–Ta–Cr–Al refractory compositionally complex alloys, Part II: high temperature oxidation behavior

Chongchong Tang, Amin Radi, Michael Dürrschnabel, Ute Jäntsch, Michael Klimenkov, Alexander Kauffmann, Martin Heilmaier, Carsten Schroer, Bronislava Gorr

PII: S2949-9178(25)00067-7

DOI: https://doi.org/10.1016/j.jalmes.2025.100217

Reference: JALMES100217

To appear in: *Journal of Alloys and Metallurgical Systems*

Received date: 20 August 2025
Revised date: 29 September 2025
Accepted date: 10 October 2025

Please cite this article as: Chongchong Tang, Amin Radi, Michael Dürrschnabel, Ute Jäntsch, Michael Klimenkov, Alexander Kauffmann, Martin Heilmaier, Carsten Schroer and Bronislava Gorr, Design of lightweight high temperature structural materials based on Ti–Mo–Ta–Cr–Al refractory compositionally complex alloys, Part II: high temperature oxidation behavior, *Journal of Alloys and Metallurgical Systems,* (2025) doi:https://doi.org/10.1016/j.jalmes.2025.100217

Design of lightweight high temperature structural materials based on Ti–Mo–Ta–Cr–Al refractory compositionally complex alloys, Part II: high temperature oxidation behavior

Chongchong Tang[a*], Amin Radi[a], Michael Dürrschnabel[a], Ute Jäntsch[a], Michael Klimenkov[a], Alexander Kauffmann[b], Martin Heilmaier[a], Carsten Schroer[a], Bronislava Gorr[a*]

[a] Karlsruhe Institute of Technology (KIT), Institute of Applied Materials (IAM), Kaiserstraße 12, 76131 Karlsruhe, Germany

[b] Ruhr University Bochum (RUB), Institute for Materials (IM), Universitätsstraße 150, 44801 Bochum, Germany

Corresponding authors: Chongchong Tang (chongchong.tang@kit.edu), Bronislava Gorr (bronislava.gorr@kit.edu)

Abstract

Three Ti-rich Ti–Mo–Ta–Cr–Al Refractory Compositionally Complex Alloys (RCCAs) with low density of ~7.5 g/cm³, identified in Part I for their stable single-phase disordered A2 structure, with room-temperature compressive plasticity and exceptional strength retention up to 1000 °C, are investigated here for their high-temperature oxidation behavior. Isothermal oxidation experiments from 800 to 1100 °C revealed the formation of multilayered oxide scales comprising four sublayers with rutile- and corundum-structured oxides. Mo initially precipitates as metallic particles within the inner oxide layer before undergoing oxidation and volatilization. Volatilization of MoO_3 becomes noticeable at temperatures above 900 °C, occurring more locally with lower Mo content. Two primary oxide scale degradation mechanisms were identified: localized scale disruption from Mo oxide volatilization and oxide scale spalling due to excessive TiN precipitation. The findings highlight the need for careful compositional balancing of Mo and Ti in these Ti-rich RCCAs to enhance oxidation resistance by simultaneously suppressing Mo-oxide volatilization and internal nitridation. Overall, they exhibit improved oxidation performance compared to conventional TiAl-based alloys and display oxidation kinetics comparable to equimolar TaMoCrTiAl at elevated temperatures.

Keywords

Ti–Mo–Ta–Cr–Al alloys; high-temperature oxidation; complex oxides; oxide volatilization; internal nitridation

1. Introduction

Refractory high-entropy alloys (RHEAs) or compositionally complex alloys (RCCAs), have emerged as promising candidates for high-temperature applications due to their high solidus temperatures, excellent high-temperature mechanical properties, and potential oxidation resistance [1–3]. Despite the well-known poor oxidation resistance of refractory metals, RCCAs in the Ta–Mo–Cr–Ti–Al system possess surprisingly high oxidation resistance, protected by complex rutile-structured Cr–Ta-based oxide scales [4,5]. A range of alloys from this system has been systematically studied regarding their phase constitution [6–9], microstructural evolution [10,11], mechanical performance [12,13], and high-temperature oxidation behavior [4,14,15]. Four principal phases are known to form in this system within the temperature range of 600 to 1300 °C: (1) disordered BCC A2 phase (W prototype), (2) ordered B2 phase (CsCl prototype), (3) Cr_2Ta-derived Laves phase (C14, C15 and C36-type), and (4) $AlMo_3$-derived A15 phase (Cr_3Si prototype) [7]. Among the alloying elements, Cr primarily promotes the formation of the Cr_2Ta-derived Laves phase, while high Al content induces a second order phase transformation from disordered A2 at high temperatures to ordered B2 at low temperatures or phase separation to A2+B2 microstructures [10,11]. In contrast, Ti addition (plus Mo and Ta) favors the stabilization of the disordered A2 phase over the ordered B2 structure [11,16].

High-temperature oxidation resistance is a critical performance criterion for materials intended for use in harsh environments. Traditional high-temperature alloys typically rely on the formation of a dense, adherent Cr_2O_3, Al_2O_3, or SiO_2 scale to protect the matrix from rapid oxidation-induced degradation [17]. Equimolar TaMoCrTiAl alloy demonstrates unexpectedly excellent oxidation resistance across a broad temperature range (500–1500 °C) attributed to the formation of an adherent, slow-growing $(Cr,Ta)O_2$-based oxide layer (accompanied by surface layers of TiO_2 and Al_2O_3). This rutile-structured $(Cr,Ta)O_2$ phase exhibits higher thermodynamic stability than the well-known Cr_2O_3 phase [4]. It can effectively block outward cation diffusion, with scale growth

predominantly controlled by inward oxygen diffusion and growth rate lies between those characteristics of Cr_2O_3 and Al_2O_3 scales [18]. Specifically, Cr and Ta (at concentrations of ~15 at% each) promote the development of protective Cr–Ta-based oxide scale [19], while Al facilitates their formation by accelerating the nucleation of Cr_2O_3 [20]. Ti has also been found to dissolve into these complex oxides and stabilize the rutile structure, contributing to the robustness of the oxide scale [4]. In addition, beneficial effects on oxidation performance have been frequently reported for conventional alloys containing both Cr and Ta when they can form a continuous $(Cr,Ta)O_2$ sublayer at high temperatures [21–23].

Composed primarily of refractory elements, RCCAs inherently face challenges among high density, poor room-temperature plasticity, and, in the case of compositions that are deformable at low temperatures, limited oxidation resistance [24–28]. Equimolar TaMoCrTiAl alloy exemplifies this challenge: despite its excellent oxidation resistance, it possesses a high density (~8.6 g/cm³) and exhibits brittleness at room temperature (due to the coexistence of ordered B2 matrix + Cr_2Ta Laves phase) [8]. To overcome these limitations, the design strategy, detailed in Part I, focuses on limiting Al content to <7 at%, while keeping Ta and Cr concentrations at moderate levels (~15 at%) and increasing Ti content to above 40 at% to develop Ti-rich RCCAs. This compositional approach aims to: (1) stabilize the single-phase disordered BCC (A2) matrix to enhance ductility while maintaining high temperature strength (Ta and Mo additions); (2) reduce density to ~7.5 g/cm³; and (3) promote the formation of protective rutile-structured Cr–Ta-based oxides for high-temperature oxidation resistance.

Titanium aluminide (TiAl)-based alloys (e.g., Ti-48Al-2Cr-2Nb) are material choices for intermediate-temperature applications (up to ~700 °C) in aerospace and automotive industries because of their low density and high specific strength. However, their intrinsic brittleness at room temperature and accelerated oxidation at higher temperatures remain major obstacles to broader implementation [29,30]. While Ni-based superalloys remain the benchmark materials for structural applications beyond 1000 °C, albeit at much higher density [31]. There remains a distinct materials gap between TiAl-based alloys and Ni-based superalloys, defined by the trade-off between low density and high-temperature capability. As aforementioned, Ti-based refractory compositionally complex alloys (RCCAs) derived from the Ta–Mo–Cr–Ti–Al system, featuring unconventional chemistries and novel oxidation protection mechanisms by $(Cr,Ta)O_2$-based complex oxides, show

promise to bridge the gap by combining relatively low density with oxidation resistance in the 700–1000 °C regime.

Guided by thermodynamic modeling, three Ti-rich TiMoTaCrAl alloys with varying Mo and Ti levels were identified and assessed in Part I for phase composition, thermal stability, and mechanical performance. Alloys were found to retain the disordered A2 structure after long-term thermal exposure, exhibit notable compressive plasticity at room temperature, and maintain exceptional strength up to 1000 °C. In this Part II study, the oxidation behavior of the same alloy set is systematically investigated in air between 800 and 1100 °C to evaluate their suitability for high-temperature structural applications. The following scientific questions are addressed: 1) Do these Ti-rich, single-phase A2 RCCAs contain sufficient Cr, Ta, and Al to foster the formation of protective Cr–Ta-based complex oxides at high temperatures? 2) How do Mo and Ti contents influence oxidation kinetics, scale microstructure, and oxide scale failure mechanisms? 3) What are the temperature limits for the long-term oxidation resistance of these Ti-rich RCCAs?

2. Materials and experiments

The three investigated alloys were synthesized via repetitive arc melting using an AM/0.5 system (Edmund Bühler GmbH, Germany) under an Ar atmosphere. High-purity bulk elements, i.e. Ta, Mo, Ti, Cr, and Al (chemPUR GmbH, Germany) with nominal metallic purities of 99.9%, 99.95%, 99.8%, 99.99%, and 99.99%, respectively, were used as raw material. The resulting cast buttons were homogenized at 1400 °C for 48 h in Ar using a resistance tube furnace with 100 K/h heating and cooling rates. Ti sponge was used as an oxygen getter to reduce the oxygen level inside the furnace during homogenization. The alloy designations, chemical compositions and impurity level are provided in Table 1. The overall chemical composition of alloy T1 (48Ti–25Mo–12Ta–10Cr–5Al) was determined by inductively coupled plasma optical emission spectrometry (ICP-OES) with an iCAP 7600 DUO device by Thermo Fisher Inc. Based on the results, complementary standard-based energy-dispersive X-ray spectroscopy (SEM-EDS) was conducted at an acceleration voltage of 20 kV (Zeiss EVO50). The total impurity concentrations of N and O were quantified via carrier gas hot extraction using a TC600 by LECO Corporation. The actual chemical compositions of the alloys agree with their designated compositions within experimental uncertainty of synthesis and chemical composition analysis. The O and N impurity levels in the

alloys are notably low, measuring below 0.1 at% and 0.03 at%, respectively (see Table 1). Experimental density measurements were carried out according to the Archimedes principle in ethanol at room temperature, following established protocols.

Coupons with approximate dimensions of (5 × 5 × 3) mm^3 were sectioned from the homogenized buttons, ground with SiC paper up to 2500 grit, and ultrasonically cleaned in ethanol to remove surface contaminants prior to high-temperature oxidation testing. Isothermal oxidation experiments were conducted using a NETZSCH STA 449 F3 Jupiter simultaneous thermal analyzer (STA) at temperatures ranging from 800 to 1100 °C in synthetic air for 48 h. Samples were heated in a flowing Ar atmosphere from room temperature to the targeted test temperature at a rate of 25 K/min. Upon reaching the desired temperature, the system stabilized for 10 min to ensure uniform temperature distribution. Synthetic air (N_2 + ~20 vol% O_2) was then introduced into the reaction chamber at a flow rate of 100 ml/min to initiate oxidation. After the designated exposure period, the air flow was stopped, and the samples were cooled to room temperature in Ar at a rate of 50 K/min. Mass changes during the exposure were continuously monitored using the integrated balance of the STA system.

X-ray diffraction (XRD) analysis was performed using a Seifert PAD II diffractometer to characterize the constituting phases in their homogenized state and post-oxidation. A Bragg-Brentano (θ-2θ) geometry was employed with a step size of 0.01° and a scan speed of 1°/min, utilizing Cu $K\alpha_1$ radiation (λ = 0.15406 nm). Scanning electron microscopy (SEM) with energy-dispersive X-ray spectroscopy (EDS) was conducted using Philips XL30S and JEOL JSM6400 instruments to investigate the surface morphology, cross-sectional structure, and chemical composition of both unoxidized and oxidized samples. For cross-sectional analysis, specimens were embedded in epoxy resin and polished using SiC paper and diamond suspensions following standard metallurgical procedures. The total oxide scale thickness, individual sublayer thicknesses and internal corrosion zone thickness were measured from backscattered electron (BSE) images using ImageJ software. Average values and standard deviations were calculated based on at least 15 measurements taken at multiple positions on each sample.

A detailed nanoscale investigation of the oxide scale structure and composition was performed on alloy T2, which was selected as a representative case due to its favorable oxidation behavior, using scanning transmission electron microscopy (STEM). Cross-sectional lamellae were prepared via

focused ion beam (FIB) technique and thinned using Ga ion milling at 30 kV within a Zeiss Auriga workstation. TEM analysis was conducted with a Talos F200X (Thermo Fisher Inc.) at an acceleration voltage of 200 kV. Selected area electron diffraction (SAED), bright-field (BF)/dark-field (DF), and high-angle annular dark-field (HAADF) imaging techniques were employed to characterize the nanoscale features.

Table 1 Designation, chemical composition and density of the three alloys.

Designation		Concentration (at%)							Density (g/cm^3)
		Ti	Mo	Ta	Cr	Al	O	N	
T1	Des.	48.0	25.0	12.0	10.0	5.0	–	–	
	Exp.	47.8	25.0	11.9	9.7	5.2	0.074	<0.023	7.5
T2	Des.	44.0	20.0	15.0	15.0	6.0	–	–	
	Exp.	44.3	20.2	15.1	14.5	5.8	0.053	<0.008	7.7
T3	Des.	54.0	10.0	15.0	15.0	6.0	–	–	
	Exp.	54.1	10.1	15.3	14.8	5.6	0.075	<0.012	7.2

3. Results

3.1. Isothermal oxidation kinetics

Figure 1 illustrates the specific mass changes of the three alloys during isothermal exposure to synthetic air from 800 to 1100 °C for 48 h. The solid lines represent data points recorded by the thermogravimetric system, while the dotted lines depict fits derived using the parabolic rate law following subsequent equation:

$$\left(\frac{\Delta W}{A}\right)^2 = K_p \times t \quad (1)$$

Here, $\Delta W/A$ represents the mass change per unit area, K_p is the parabolic rate constant, and t is time. The experimentally recorded final mass gains and calculated parabolic rate constants are summarized in Table 2. All mass change data can be fitted by parabolic rate law with medium or high coefficients of determination (R^2). Mass gain generally increases in the order of T1 to T3 at

900, 1000 and 1100 °C, while at 800 °C T3 exhibits the lowest mass gain. The highest mass gain of 5.80 mg/cm^2 was observed for T3 after oxidation at 1100 °C for 48 h.

However, anomalous phenomena were observed, notably that the mass gains do not consistently increase with increasing oxidation temperature for individual alloys. This effect is particularly pronounced in alloy with higher Mo content, namely T1. More specifically, for alloy T1 the mass gain at 800 °C exceeds those at 900 and 1000 °C, while for T2, the mass gain at 800 °C surpasses that at 900 °C. In contrast, only T3 shows a progressive increase in mass gain with increasing oxidation temperature. Subsequent microstructural investigations reveal that this anomalous behavior stems from the volatilization of MoO_3, which intensifies with higher Mo concentration (see subsequent Section 3.3.2 for details). Log–log plots of mass change versus exposure time reveals irregular, slight decreases in slope particularly after prolonged exposure at high temperatures, suggesting oxide volatilization (Supplementary Fig. S1). Values italicized in Table 2 denote cases where substantial MoO_3 volatilization occurs with simultaneous mass loss, rendering the mass gain data unrepresentative of intrinsic oxidation resistance (i.e., 900, 1000, and 1100 °C for T1; 900 and 1000 °C for T2; 1000 °C for T3). For other conditions, MoO_3 volatilization is considered negligible as affirmed by subsequent oxide scale structure and thickness investigations. Therefore, when assessing their intrinsic oxidation resistance and ranking alloy oxidation performance, mass gains are unreliable considering oxide volatilization and/or scale failure; a more representative parameter is the total corrosion depth (see Discussion section).

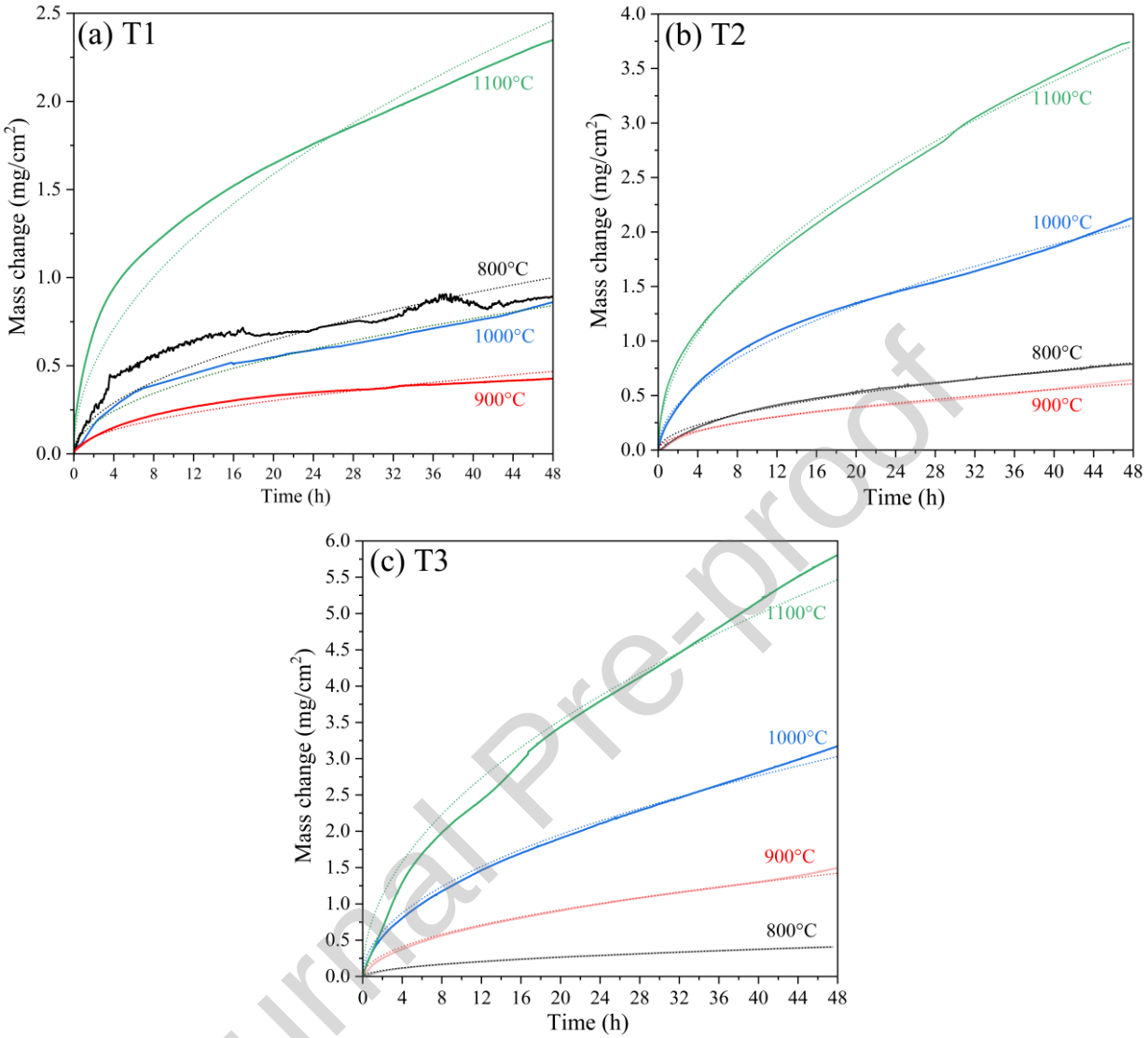

Fig. 1 Mass change curves (solid lines) and parabolic law fitting (dotted lines) for the three alloys during oxidation at 800 to 1100 °C in synthetic air for 48 h. (a) T1, (b) T2, (c) T3. Note the scale on the mass change axis is different from (a) to (c).

Table 2 Experimentally recorded mass gain and calculated parabolic rate constants with coefficient of determination (R^2) after 48 h oxidation in synthetic air (The numbers in italics/bold cannot represent the intrinsic oxidation resistance of the alloys owing to substantial MoO_3 volatilization with mass loss and/or scale failure).

	Alloy	800 °C	900 °C	1000 °C	1100 °C
Mass gain (mg/cm²)	**T1**	0.89	***0.43***	***0.86***	***2.35***
	T2	0.79	***0.64***	***2.13***	3.74
	T3	0.41	1.49	***3.17***	5.80
Parabolic rate constant (K_p: $kg^2 \cdot m^{-4} \cdot s^{-1}$) and Coefficient of determination (R^2)	**T1**	5.80×10^{-10}	$\boldsymbol{1.27\times10^{-10}}$	$\boldsymbol{4.10\times10^{-10}}$	$\boldsymbol{3.50\times10^{-9}}$
		0.76	0.94	0.98	0.94
	T2	3.71×10^{-10}	$\boldsymbol{2.14\times10^{-10}}$	$\boldsymbol{2.47\times10^{-9}}$	7.95×10^{-9}
		0.99	0.99	0.99	0.99
	T3	9.72×10^{-11}	1.17×10^{-9}	$\boldsymbol{5.31\times10^{-9}}$	1.73×10^{-8}
		0.99	0.99	*0.99*	0.98

3.2. Phase composition of oxide scales

The phase composition of the oxide scales identified by XRD is presented in Fig. 2. Two primary oxide crystal structures are detected: corundum (Al_2O_3 prototype, $D5_1$, space group *R-3c*) and rutile (TiO_2 prototype, C4, space group *$P4_2/mnm$*). The diffraction peaks corresponding to corundum exhibit significantly lower intensity and shift slightly toward lower 2θ angles (compared to pure Al_2O_3). This shift suggests formation of $(Cr,Al)_2O_3$ solid solutions (confirmed later by SEM and TEM analyses), which are commonly observed during oxidation of alloys containing both Al and Cr [32–34]. The corundum phase constitutes the minor component, while the majority phase is rutile.

A closer examination of the diffraction peaks assigned to rutile structure reveals two distinct, separable peaks, as exemplified for T2 in Fig. 2(b). Several ternary or more complex oxides with rutile structure relevant to this system exist [4], notably $(Cr,Ta)O_2$ and $(Ti,Ta)O_2$ solid solutions. The lattice parameters of these oxides are as follows: for $(Cr,Ta)O_2$ (PDF No. 39-1428), *a* 4.6417 Å, *c* 3.0199 Å; for $(Ti,Ta)O_2$ (PDF No. 33-1386), *a* 4.6953 Å, *c* 3.0659 Å. These values are larger than those of pure rutile TiO_2 (*a* 4.5928 Å, *c* 2.9582 Å). Consequently, Peak 1 at lower 2θ angles,

marked in Fig. 2(b), can be attributed to these complex oxides with rutile structure, which can form solid solutions with varying concentrations. Peak 2, observed at higher 2θ angles, corresponds to the pure TiO_2 phase. Subsequent cross-sectional investigations further confirm the presence of a surface TiO_2 layer and inner layers of complex oxides with rutile structure (see Section 3.3).

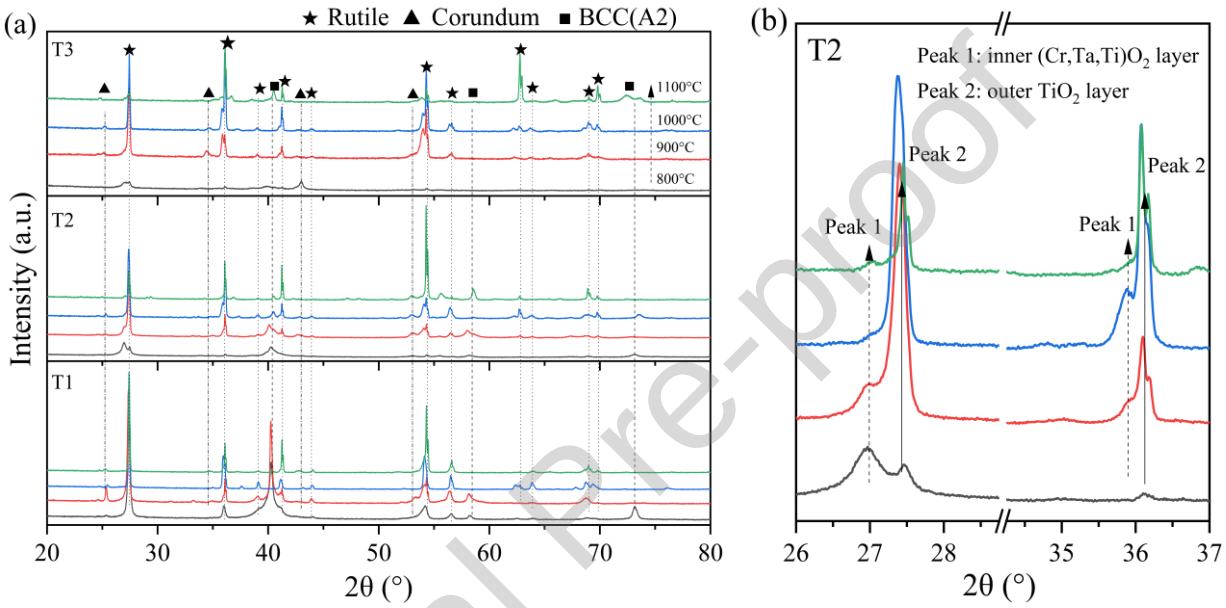

Fig. 2 XRD patterns for the three alloys after oxidation from 800 to 1100 °C in synthetic air for 48 h. (a) All three alloys, (b) detailed view of XRD patterns of T2 alloys within the 2θ range of 26 to 37°.

3.3. Microstructure and composition of oxidized alloys

3.3.1. Surface morphology

Typical surface images of the oxide scales formed on the alloys after oxidation are presented in Fig. 3 for T1. The oxide scales on T2 and T3 appear morphologically similar, except for distinct macroscopic features observed at higher temperatures (1000 and 1100 °C); therefore, their images are provided in Supplementary Information (Fig. S2 and Fig. S3). The oxide scales exhibit characteristic, predominantly equiaxed grains, and sometimes straight-sided, faceted morphologies. Enlarged surface imaging in the upper right corner reveals that the oxide scales lack a fully compact structure, with visible gaps between adjacent grains. However, for all alloys, the oxide scales become denser and exhibit larger grain sizes on the outer surface as the oxidation

temperature increases. EDS analysis indicates that the surface oxide scales primarily consist of Ti and O.

For T1, no oxide scale spalling was observed after oxidation across all four temperatures; however, micro-cracking was detected following oxidation at 1100 °C, as shown in Fig. 3(d). At 1000 °C, both T2 and T3 exhibit scale buckling and cracking (Figs.S2 and S3). In T2, the buckled regions display large circumferences, covering nearly 40% of total surface area and leading to scale spalling. In contrast, T3 exhibits only buckling, affecting a smaller portion of the surface (approximately 15%). At 1100 °C, the oxide scale on T2 develops a dense structure without buckling or spalling, whereas T3 undergoes substantial oxide scale spalling (Fig.S3).

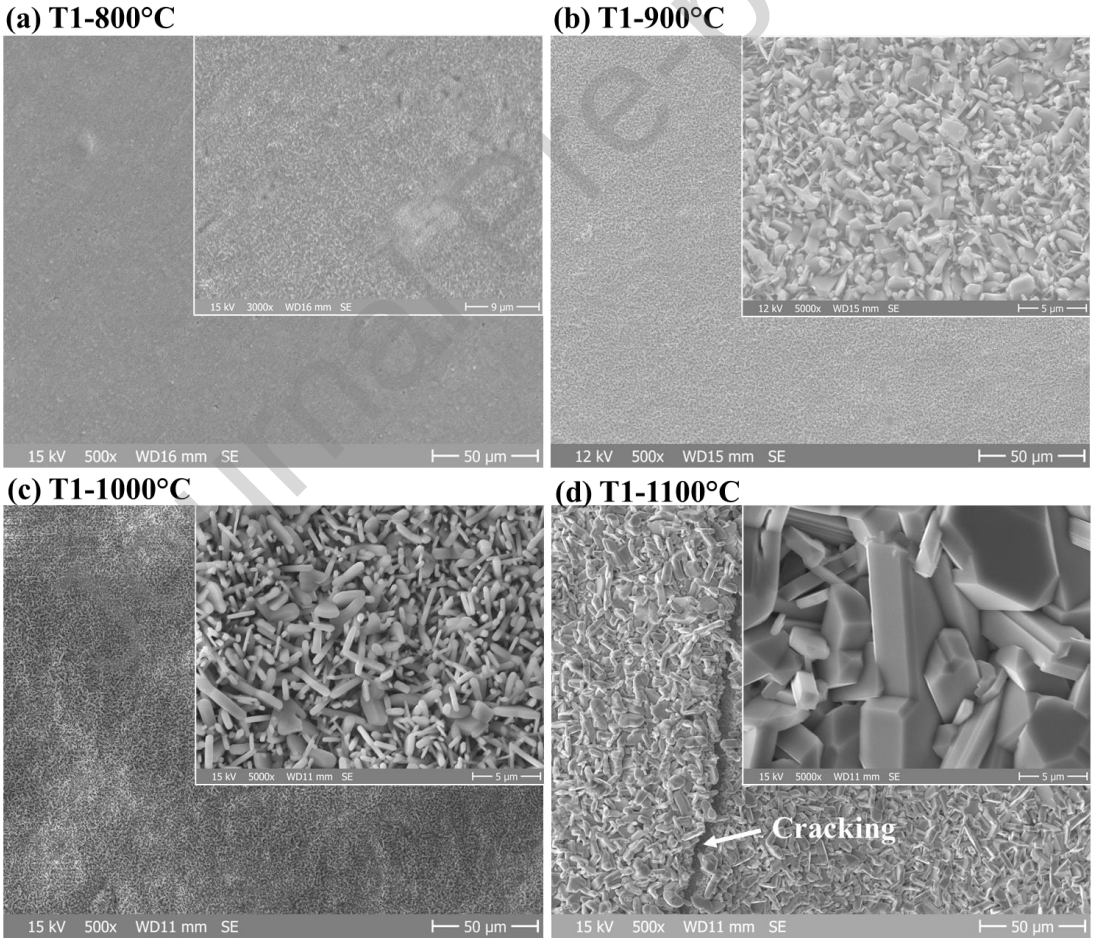

Fig. 3 Surface SEM images of T1 alloys after oxidation from 800 to 1100 °C in synthetic air for 48 h. (a) 800 °C, (b) 900 °C, (c) 1000 °C, (d) 1100 °C. The images inserted in the upper right corner are taken at higher magnifications.

3.3.2. Cross-sectional microstructure by SEM

Figure 4 illustrates representative cross-sectional microstructures of oxide scales and scale/alloy interfaces of T1 after oxidation, with the thermally grown oxide scales and their corresponding thickness indicated at scale/alloy interfaces. Distinct oxide scale characteristics were observed following oxidation at each of the four temperatures. At 800 °C, a thin and relatively uniform oxide layer formed on the alloy surface, with no evident signs of internal corrosion. The oxide scale thickened slightly and exhibited a noticeably porous structure after oxidation at 900 °C. Needle-shaped TiN particles beneath the oxide scale were observed starting at 900 °C. At 1000 °C, a substantially thicker and porous oxide layer, exceeding 50 μm, developed with wavy interfaces. Notably, a discrepancy exists between the oxide scale thickness and the final experimentally recorded mass gain (see Table 2) across these temperatures. An oxide scale thickness of ~50 μm would correspond to an area-specific mass gain exceeding 8 mg/cm^2; however, the experimentally measured mass gain at 1000 °C was only 0.86 mg/cm^2. This observation clearly indicates that oxide volatilization (MoO_3 here) contributes to mass loss at higher temperatures, particularly since no oxide scale spalling was detected.

Additional interrupted oxidation experiments were conducted at 1000 °C for 24 h to better understand the oxide scale evolution. The resulting oxide scale structures and EDS mapping for both 24-h and 48-h exposures are presented in Fig. 5. After 24 h of oxidation, a denser and thinner oxide scale was observed, as depicted in Fig. 5(a). This oxide scale exhibits a distinct layered structure, comprising a surface layer of TiO_2 followed by solid solution $(Cr,Al)_2O_3$ layer. The mapping displays Al and Cr concentration gradients, with higher levels of Al toward the surface. Beneath the surface layers, an additional oxide sublayer enriched in Ti, Ta, and Mo is present. In contrast, after 48 h exposure, the thick, porous oxide scale consists of Ti, Cr, and Ta, with discontinuous and isolated Al-rich oxides, as shown in Fig. 5(b). EDS mapping reveals the absence of Mo within the oxide scale. These findings indicate that Mo is initially enriched in the oxide scale during the early oxidation stage, followed by progressive oxidation and volatilization.

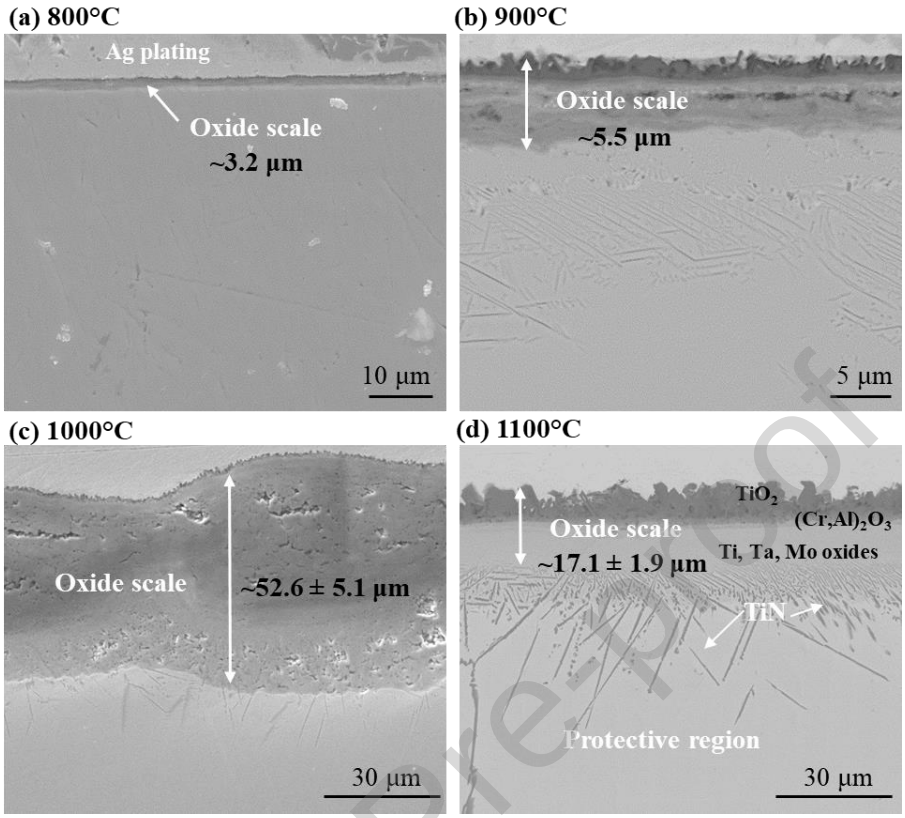

Fig. 4 Cross-sectional SEM images of T1 after oxidation in synthetic air for 48 h. (a) 800 °C, (b) 900 °C, (c) 1000 °C, (d) 1100 °C.

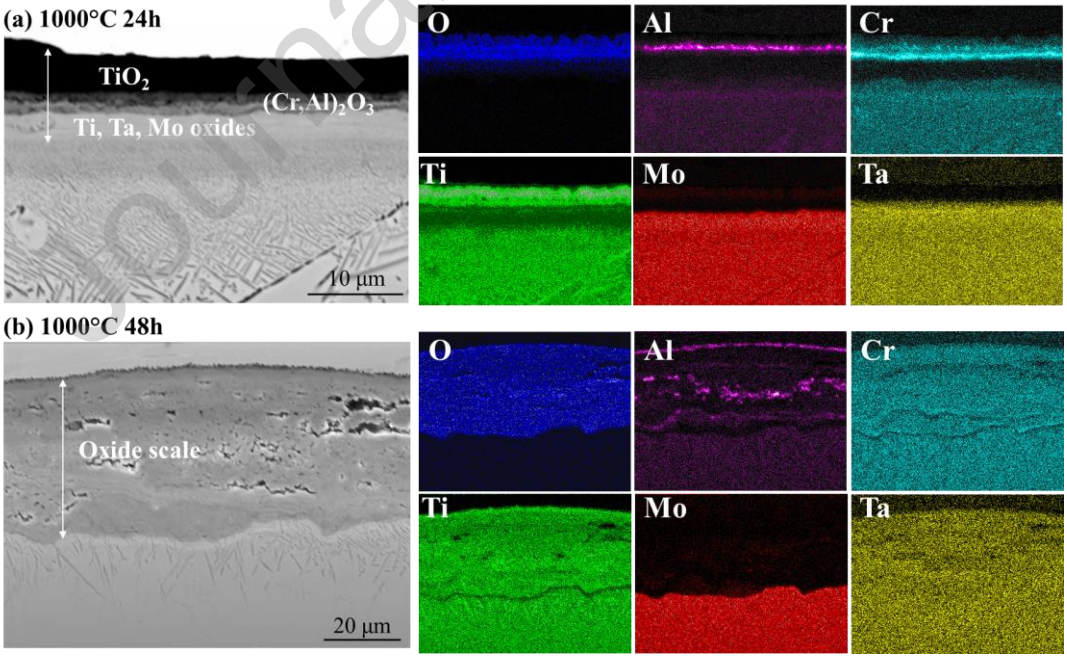

Fig. 5 Cross-sectional SEM images and corresponding EDS mapping of T1 after oxidation at 1000 °C in synthetic air. (a) 24 h, (b) 48 h.

The oxide scale formed after oxidation at 1100 °C can be classified into three distinct regions, as illustrated in Fig. 4(d) (showing the protective region) and Fig. 6 (depicting all three regions, marked as 1: protective region, 2: transition region, 3: failure region). In the protective region (see also Fig. S4 with EDS measurements), the oxide scale exhibits a dense, multilayered structure, consisting of an outer TiO_2 layer, a center $(Cr,Al)_2O_3$ layer, and an inner complex oxide layer, resembling the structure observed in Fig. 5(a). The external TiO_2 layer displays a highly convoluted border. The transition region begins with micro-cracking of the oxide scale (Fig. 3(d)), allowing direct air ingress and accelerating MoO_3 volatilization. This volatilization results in a high density of pores within the inner oxide layer, as observed in Fig. 6 of the transition region. Once Mo within the oxide scale is completely evaporated, the oxide scale is supposed to lose its protective capability, initiating the rapid growth of non-protective, porous TiO_2-based oxide scales beneath. This leads to localized failure of the oxide scale, as marked with failure region in Fig.6. Interestingly, the denser structure of oxide scale formed initially at elevated temperatures alters its failure behavior induced by Mo oxide volatilization, transitioning from global failure at 1000 °C to localized failure at 1100 °C (see Fig.3, Fig.5, and Fig.6).

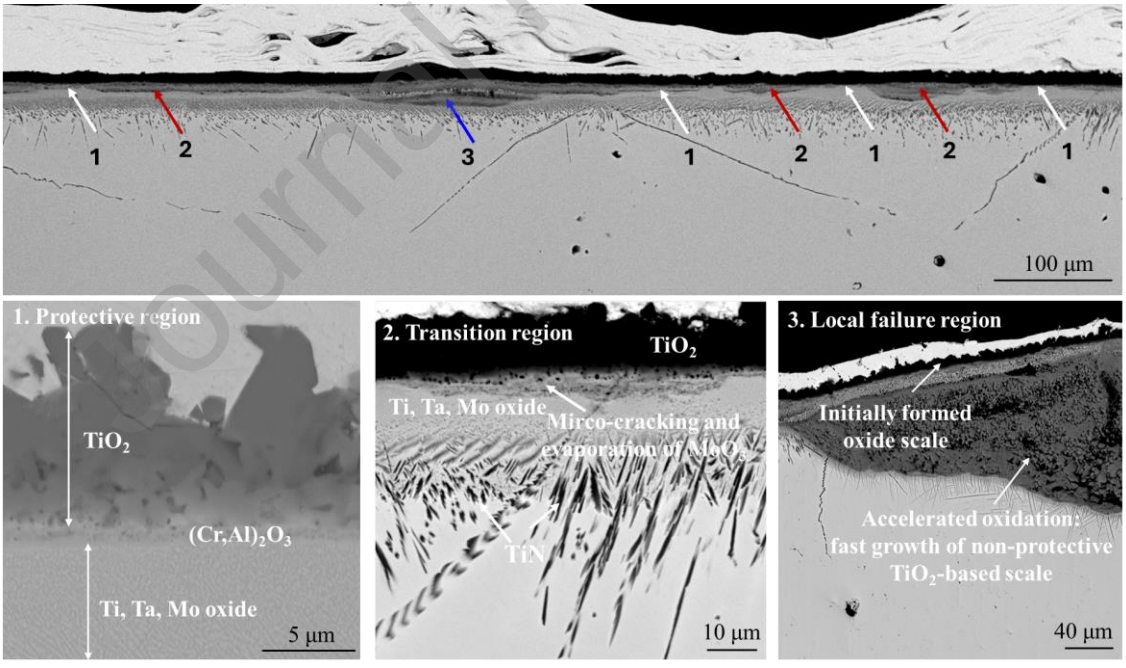

Fig. 6 Cross-sectional SEM images of T1 after oxidation at 1100 °C in synthetic air for 48 h. Three different regions are identified and marked as 1: Protective region, 2: Transition region, 3: Local failure region.

Representative oxide scale structures on alloys T2 and T3 after oxidation at 1000 and 1100 °C are shown in Fig. 7, with additional cross-sectional images for all temperatures and EDS measurements available in the Supplementary Information (Figs. S5 to S8). The oxide scales exhibit multilayered structures similar to those of T1, except that the inner complex oxide layer evolves into two sublayers: an upper Cr-Ta-Ti-rich sublayer and a lower Ti-Ta-Mo-containing sublayer (see Fig. 7(b), Fig. S7, Fig. S8, and more clearly resolved in subsequent STEM investigations). In addition, oxide scale failure occurs only locally in these two alloys as observed globally in T1 at 1000 °C, as shown in Fig. 5 and Fig. 7(a). For T3 with the highest Ti content (54 at%), extensive needle-shaped TiN particles precipitate beneath the oxide scale, driven by internal nitridation, accompanied by oxide scale spalling at the scale/alloy interface, Fig. 7(b).

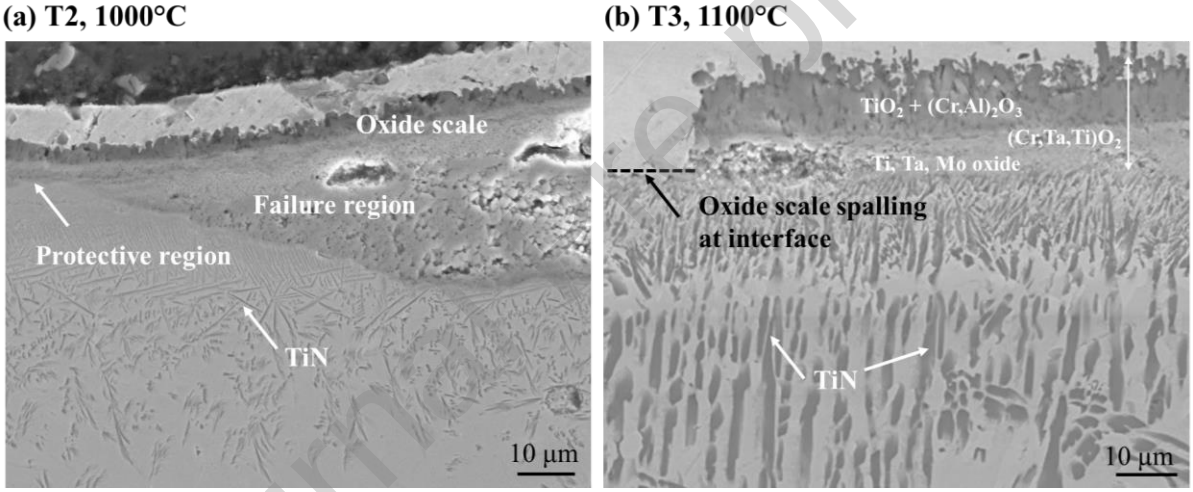

Fig. 7 Cross-sectional SEM images of T2 and T3 after oxidation in synthetic air for 48 h. (a) T2 at 1000 °C, (b) T3 at 1100 °C.

3.3.3. Oxide scale structure on T2 by STEM

Figure 8 presents the TEM-HAADF image and corresponding EDS elemental maps of alloy T2 after oxidation of 48 h at 800 °C. The oxide scale, indicated by the arrow, has a total thickness of approximately 0.9 µm and exhibits a relatively dense structure at this temperature. The nanoscale oxide sublayers, previously unresolved by SEM, are now shown to comprise four distinct layers: an outer TiO_2 layer, a thin $(Cr,Al)_2O_3$ solid solution layer (~60 nm), an intermediate $(Cr,Ti,Ta)O_2$ layer, and an innermost mixed oxide layer rich in Ti, Ta, and Mo. No evidence of nitridation was observed beneath the oxide scale at this temperature. However, nanoscale Cr_2Ta Laves phase

precipitates were detected in the substrate region below the scale, as revealed by both HAADF contrast and EDS mapping. This is consistent with Part I study on phase stability, which shows that minor amount of C15 Laves phase forms after long-term heat treatment at 800 °C.

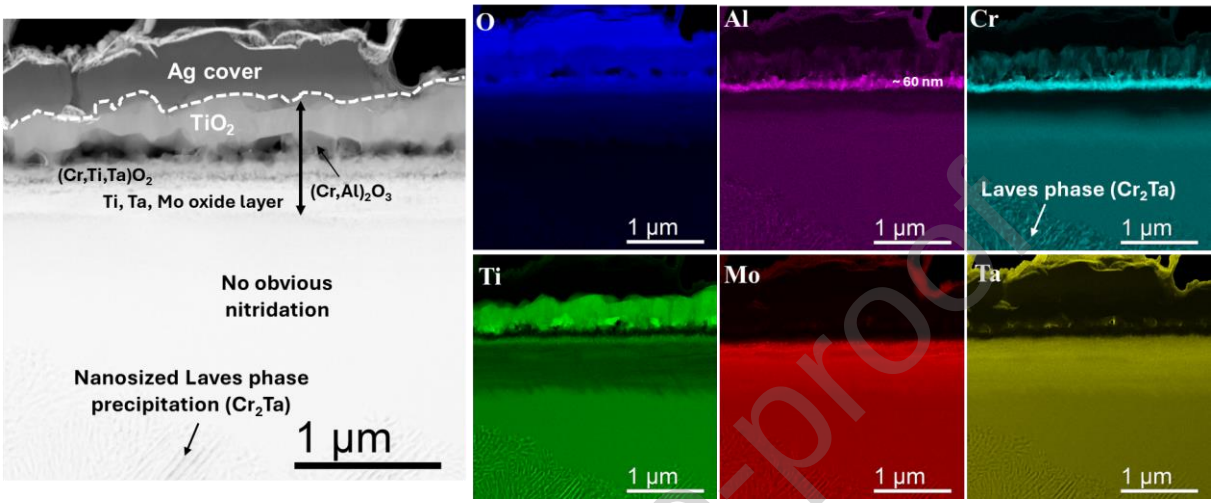

Fig. 8 TEM-HAADF and EDS mapping of T2 after oxidation in synthetic air at 800 °C for 48 h.

A general overview of the lamella prior to thinning of T2 sample after oxidation at 1100 °C, along with STEM analysis of the oxide layers, is presented in Fig. 9. Two site-specific regions were meticulously extracted and thinned for detailed examination: one located immediately beneath the surface and the other adjacent to the inner oxide layer interface, as indicated in Fig. 9(a). In these two regions, a relatively high density of pores is observed, with Area01 of Fig. 9(b) exhibiting larger pores and Area02 of Fig. 9(c) displaying finer pores, in contrast to other regions. The surface layer was affirmed as pure rutile TiO_2 layer, as substantiated by SAED in Fig. 9(b). The pores with diameters of micrometer range within this surface layer are distinctly visible. The HAADF image of Area02 and the corresponding EDS mapping in Fig. 9(d) further confirm the multilayered oxide scale with distinct sublayers: solid solution $(Cr,Al)_2O_3$ layer beneath the surface TiO_2 layer, followed by two inner, rutile-structured complex oxide sublayers, $(Cr,Ta,Ti)O_2$ and $(Ti,Ta)O_2$. Nano-sized pores are predominantly located near the interface between the two complex oxide layers and extend into the inner $(Ti,Ta)O_2$ layer, Fig.9(c). Additional STEM-EDS mapping and EDS line profiles across the $(Cr,Al)_2O_3$/$(Cr,Ta,Ti)O_2$ interface and within the $(Ti,Ta)O_2$ layer are presented in Fig.10. As shown in Fig.10(a), the $(Cr,Ta,Ti)O_2$ layer consists of approximately 15.5%

Ti, 11.5% Ta, and 8.0% Cr. Some inclusions, primarily Cr_2O_3 and Ta_2O_5, are also present in this layer, possibly unreacted and not fully dissolved into the rutile-structured complex oxides (Fig.S9). The inner $(Ti,Ta)O_2$ layer displays a stoichiometry with nearly equal Ti and Ta concentrations (can also be denoted as $TiTaO_4$ [35]).

Mo-rich particles are primarily observed within the inner $(Ti,Ta)O_2$ layer. The SAED pattern in Fig. 9(d) reveals that these Mo-rich particles are metallic Mo precipitates rather than Mo oxides. EDS line scanning across several Mo-rich particles (Fig. 10(b)) confirms their Mo concentrations reaching up to 80 at%. These Mo particles exhibit the same crystallographic orientation within the analyzed region. Their volume density and size increase as the oxide layer approaches the alloy matrix.

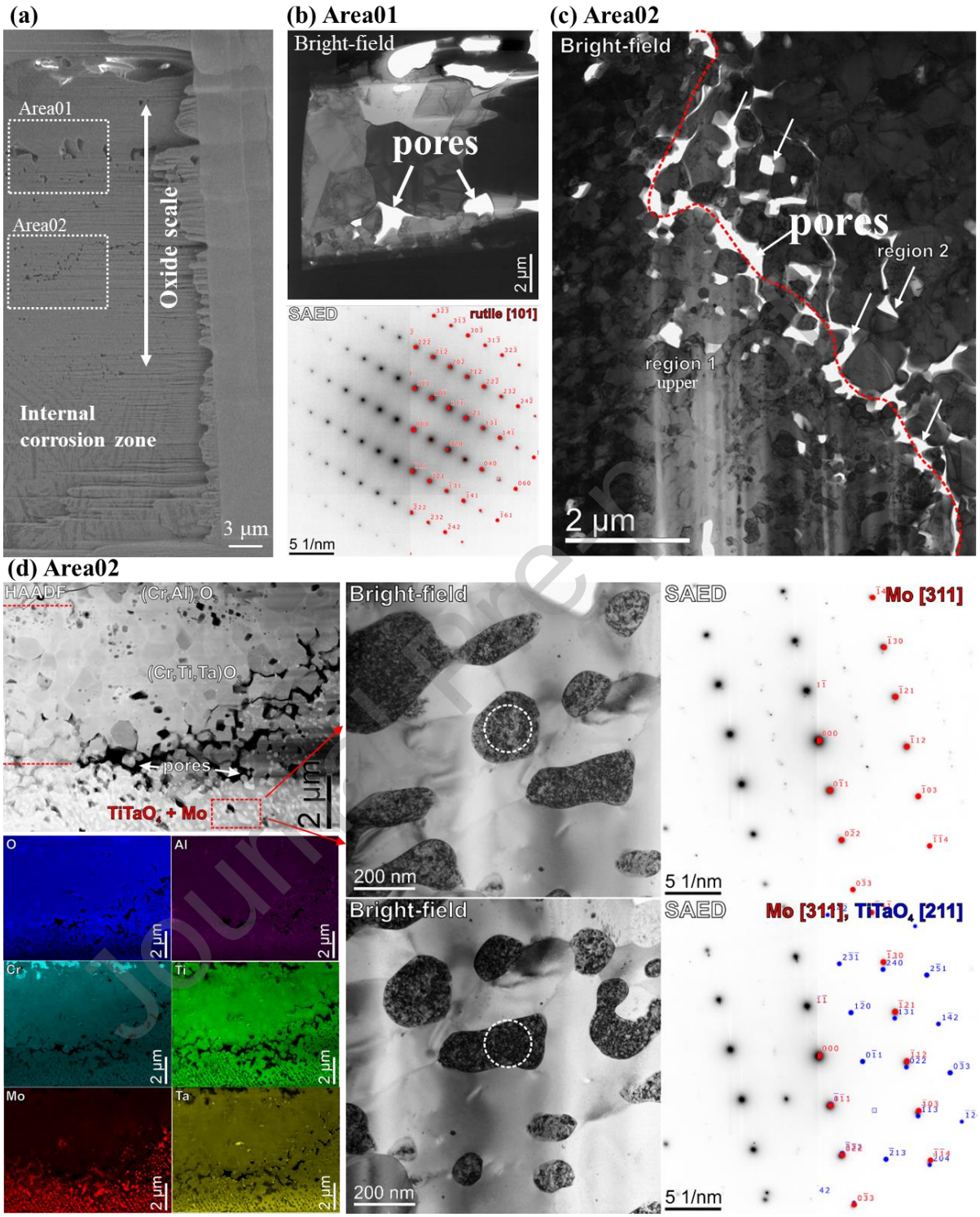

Fig. 9 TEM results of T2 after oxidation in synthetic air at 1100 °C for 48 h. (a) Lamella prepared by FIB with two distinct areas (Area01 and Area02) selected for TEM investigations, (b) BF and SAED of Area01, (c)BF of Area02 highlighting the pores at oxide sublayer interface, (d) HAADF, elemental mapping and two bright-field images with corresponding SAED of the inner oxide layer.

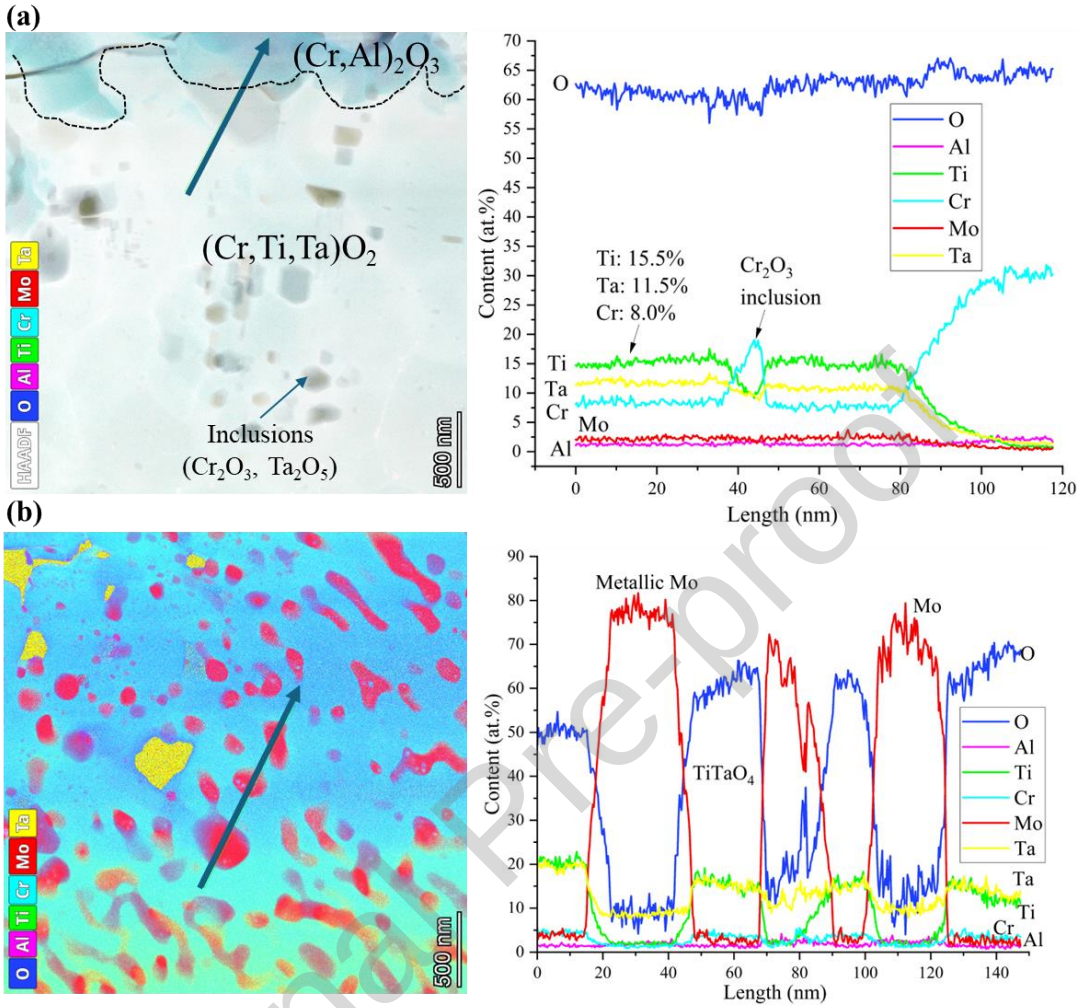

Fig. 10 STEM-EDS mapping and EDS line-profiles along the arrow of T2 after oxidation in synthetic air at 1100 °C for 48 h. (a) at upper $(Cr,Al)_2O_3/(Cr,Ta,Ti)O_2$ interface, (b) within the inner $(Ti,Ta)O_2$ layer.

4. Discussion

4.1. Oxide scale growth and failure mechanisms

The microstructure of the thermally grown oxide scales on the Ti-rich TiMoTaCrAl alloys (prior to scale failure) resembles those formed on equimolar TaMoCrTiAl alloys [4,19]. One notable distinction is: while the surface oxide layer on equimolar TaMoCrTiAl alloys consists of a mixture of rutile TiO_2 and solid solution $(Cr,Al)_2O_3$, the alloys investigated here form an exclusively TiO_2 surface layer with a thin underlying $(Cr,Al)_2O_3$ layer. Figure 11 presents the schematic illustration of the oxide scale structure on the Ti-rich TiMoTaCrAl alloys following high-temperature oxidation in air. The formation of a surface layer consisting exclusively of TiO_2 can be attributed to the significantly higher Ti concentration (> 44 at%) and rapid growth kinetics of the less-protective rutile TiO_2 scale [36,37]. It is well-established that rutile TiO_2 scales primarily grow through the outward diffusion of Ti ions [36–38]. The highly coarsened surface morphology of the outmost TiO_2 layer (Fig.6 and Fig.7) supports this outward growth mechanism. Its rapid growth kinetics result in a high density of pores/cavities within the layer, a phenomenon also consistently reported, for instance, during the oxidation of TiAl alloys [36,39].

The standard Gibbs free energies of formation for the oxides involved in this study at 900 °C are as follows: Al_2O_3: -869 kJ/mol O_2, TiO_2 (rutile): -732 kJ/mol O_2, Ta_2O_5: -612 kJ/mol O_2, and Cr_2O_3: -555 kJ/mol O_2. In contrast, MoO_2 (s) and MoO_3 (s) exhibit significantly lower thermodynamic stability, with values of -376 kJ/mol O_2 and -304 kJ/mol O_2, respectively (see Ellingham diagram of Fig. S10). Because of the porous structure of the surface TiO_2 layer, the oxygen partial pressure underneath is high enough for oxidation of Al, Cr and Ta. The reaction between Al_2O_3 and Cr_2O_3 forms the $(Cr,Al)_2O_3$ solid solution, while the interaction of TiO_2, Cr_2O_3, and Ta_2O_5 produces a rutile-structured $(Cr,Ta,Ti)O_2$ layer beneath [4]. The oxidation process will be dominated by inward diffusion of anions following the establishment of a continuous rutile-structured $(Cr,Ta,Ti)O_2$ layer [18,19,21,40]. Compared to T2 and T3, the $(Cr,Ta,Ti)O_2$ layer on T1 (Fig.6) cannot be clearly distinguished by SEM, possibly due to its low thickness because of the lower Cr content in this alloy (10 at% vs 15 at%). The formation of an inner $(Ti,Ta)O_2$ layer beneath the $(Cr,Ta,Ti)O_2$ layer can be explained by two key factors: depletion of Cr beneath the oxide scale within the alloy matrix and lower thermodynamic stability of Cr_2O_3 compared to TiO_2 and Ta_2O_5. As illustrated in Fig. S7, the Cr concentration within the alloy matrix (T2, after oxidation at

1100 °C) beneath the oxide scale is approximately 3 at%, significantly lower than that of Ti (15–20 at%), Ta (5–8 at%), and Mo (8–10 at%). Thermodynamic calculations also demonstrate that $(Ti,Ta)O_2$ is more stable than $(Cr,Ta,Ti)O_2$, assuming these complex oxides form from simple binary oxides [35]. These two reasons suggest that, over time, Ti and Ta are preferentially oxidized to form the inner $(Ti,Ta)O_2$ layer.

The rutile-structured $(Cr,Ta,Ti)O_2$ exhibits n(negative)-type conductivity, with oxygen vacancies as the dominant defects, enabling readily oxygen diffusion via the anion sublattice [4,21]. Our previous investigations confirmed the presence of cations in the oxidation states Cr^{3+}, Ti^{4+}, and Ta^{5+} in $(Cr,Ta,Ti)O_2$, and suggest that Ti^{4+} cations are likely incorporated on Cr^{3+} lattice sites, thereby reducing the oxygen vacancy concentration [4]. The precise oxidation states of Ti and Ta atoms in the inner $(Ti,Ta)O_2$ layer have not yet been conclusively determined. Given that Ti^{4+} and Ta^{5+} have higher oxidation states than Cr^{3+}, their substitution for Cr^{3+} would be expected to further suppress oxygen vacancy formation in $(Ti,Ta)O_2$, potentially decreasing the diffusivity of both oxygen and nitrogen. This assumption is supported by previous oxidation studies on Ni-based superalloys [41], which reported that the $(Ti,Ta)O_2$ layer hinders outward cation diffusion and reduces inward oxygen flux, thereby improving oxidation resistance. A more detailed investigation of the defect chemistry and diffusivities within the inner $(Ti,Ta)O_2$ layer is therefore required in future studies.

Given that Mo requires a substantially higher oxygen partial pressure for oxidation, it is reasonable to infer that it precipitates as metallic particles following the selective oxidation of other elements. The high density of nanoscale pores at the $(Cr,Ta,Ti)O_2$/$(Ti,Ta)O_2$ interface, as observed in Fig. 9(c), indicates that Mo can escape from the oxide scale via formation of gaseous MoO_3 [42,43]. Since the oxide scale is not dense and contains pores/cavities, the oxygen partial pressure in the vicinity of these defects can elevate sufficiently to oxidize Mo into volatile MoO_3. To support this claim, the partial pressure of gaseous MoO_3 was estimated at varying oxygen partial pressures based on the following reaction:

$$2/3\ Mo\ (s) + O_2\ (g) = 2/3\ MoO_3\ (g) \quad (2)$$

The standard Gibbs free energy change for oxide formation at a given temperature is expressed as: $\Delta G^{\circ} = -RT \ln K$, where K is the equilibrium constant with $K = a_{MoO3}^{\frac{2}{3}}/(a_{Mo}^{\frac{2}{3}} \cdot P_{O2})$ here. With a Gibbs free energy of formation of –200.5 kJ/mol O_2 for MoO_3 (g) at 900 °C (see Ellingham diagram of Fig. S10), the corresponding equilibrium partial pressure of MoO_3 (g) can be calculated. It has been suggested that vapor pressures on the order of 10^{-6} bar is sufficient to induce noticeable oxide volatilization and significant material loss [44]. At a MoO_3(g) vapor pressure of 10^{-6} bar, and assuming the chemical activity of Mo to be unity (since Mo precipitates as metallic particles before oxidation), the calculated equilibrium constant for reaction (2) at 900°C is 8.6×10^{8}. This corresponds to an oxygen partial pressure of 1.2×10^{-13} bar, which is higher than the equilibrium oxygen partial pressure of Cr_2O_3 (10^{-17} bar at 900°C), yet represents a very low oxygen level. Since oxygen partial pressures within interconnected pores are generally elevated and may reach levels exceeding 10% of the ambient pressure [45], the formation of gaseous MoO_3 is therefore expected in the vicinity of pores. The gaseous MoO_3 phase can then escape through pre-existing pores or micro-cracks. Micro-cracking of the oxide scale normally arises from stress accumulation within the scale [46,47], here associated with the growth of binary Ta_2O_5 inclusions of a high Pilling–Bedworth Ratio (PBR, 2.59) [48] and/or oxide scale thickening. The oxidation and subsequent evaporation of Mo will generate additional pores, creating new surfaces that further accelerate this process. This mechanism appears to contribute to the global failure of the oxide scale on T1 at 1000 °C after 48 h of oxidation, particularly given its high Mo content (Fig. 5). For T2 and T3, which have lower Mo contents, micro-cracking of the oxide scale similarly enhances evaporation, leading to localized failure once Mo particles within the inner oxide layer are depleted (Fig. 7). The reduced volatilization kinetics of MoO_3 at lower oxidation temperatures (800 and 900 °C) apparently have not triggered macro-level failure of the oxide scale after 48 h of exposure. Intriguingly, at an elevated temperature of 1100 °C, the formation of a denser oxide scale with larger grains appears to alleviate Mo evaporation (Fig. 3 (d) and Fig. 9), thereby extending the protective period of the scale.

The Mo particles within the inner complex oxide layer exhibit a preferred crystallographic orientation (see Fig. 9). This orientation likely originates from large matrix grains after selective oxidation of other elements, aligning preferentially with the surrounding oxides to minimize

interfacial energy. However, its potential implications for diffusion pathways and pore nucleation remain unclear and warrant further investigation. Nitrogen diffusion through the oxide scale causes internal nitridation, leading to TiN precipitation, like equimolar TaMoCrTiAl alloys. No significant internal oxidation of Al was observed in these alloys.

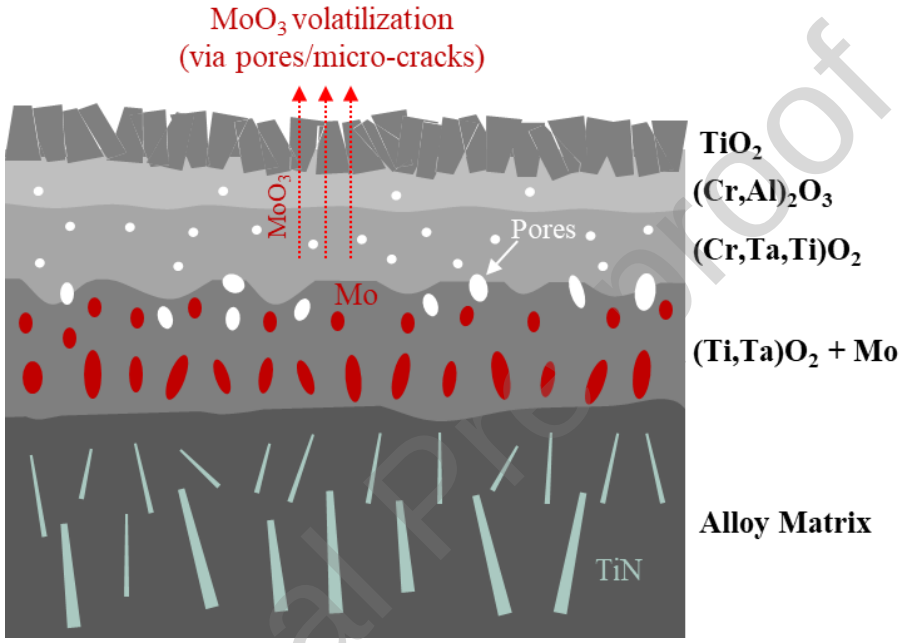

Fig. 11 Schematic illustration of the oxide scale structure on the Ti-rich TaMoCrTiAl alloys before failure. Mo precipitates as metallic particles within the inner oxide scale before undergoing oxidation and volatilization.

4.2. Effects of Mo and Ti content

Figure 12 illustrates the thicknesses of oxide scale and internal corrosion zone (ICZ), total corrosion depth, along with the contribution of MoO_3 volatilization to mass loss at 1000 °C. A cross-correlation between oxide scale thickness and experimentally recorded mass gain was conducted to evaluate the extent of MoO_3 volatilization across all alloys. The volatilization-induced mass loss was inferred from the discrepancy between the calculated mass gain (derived from oxide scale thickness) and the experimentally recorded values (Table 2). The conversion of scale thickness to calculated mass gain assumes a compact oxide scale and negligible internal nitridation (see Table S1), introducing a degree of uncertainty. Nevertheless, this approach

provides an indication of the magnitude of MoO_3 volatilization under each condition. The calculations reveal cases with substantial MoO_3 volatilization already marked in Table 2 (the corresponding mass losses are provided in Table S2).

Alloy T2 generally demonstrates the best oxidation performance with the lowest scale thickness, Fig. 12(a). No internal nitridation was observed at 800 °C for T1 and T2, whereas T3 already exhibited a TiN precipitation zone of approximately 30 μm thick, as shown in Fig. 12(b). At higher temperatures, T3 displays substantial TiN precipitation with significantly thicker ICZ and total corrosion depth (Fig. 12(b) and (c)), which correlates with its highest Ti content and lowest Mo content. A high-volume fraction of TiN precipitates likely deteriorates oxide scale adherence, leading to scale spalling in T3 after oxidation at 1100 °C (Fig.7 (b)). Spalling can be attributed to the high thermal expansion mismatch between TiN (~9.5×10^{-6} K^{-1}) [49] and complex oxides (~6×10^{-6} K^{-1}) [50], generating thermal stress of ~1.4 GPa within the oxide layer upon cooling [51] that cause oxide scale detachment. Therefore, from the perspective of oxidation resistance, T3 can be excluded from further optimization.

The ICZ thicknesses are greater in T2 at all temperatures compared to T1 (48 at% Ti), see Fig. 12(b), despite its slightly lower Ti content (44 at% Ti). It can be concluded that increasing Mo content (25 at% Mo in T1 vs. 20 at% Mo in T2) enhances the alloy's nitridation resistance, given the extremely low solubility of nitrogen in metallic Mo [52,53]. However, high Mo content evidently increases MoO_3 volatilization, as demonstrated in Fig. 12(d) for 1000 °C. The mass loss attributed to MoO_3 volatilization decreased from ~8.0 mg/cm^2 for T1 (25 at% Mo) to below 1 mg/cm^2 for T3 (10 at% Mo) after oxidation at 1000 °C for 48 h. Rapid MoO_3 volatilization leads to premature failure of the oxide scale, either globally or locally, by creating high density of pores within the inner oxide scale, as detailed in the results section. To mitigate MoO_3 volatilization and suppress internal nitridation, an optimal combination of Mo and Ti content is necessary. The findings suggest that Mo concentrations between 15–20 at% and Ti concentrations between 40–50 at% represent a delicate yet effective balance.

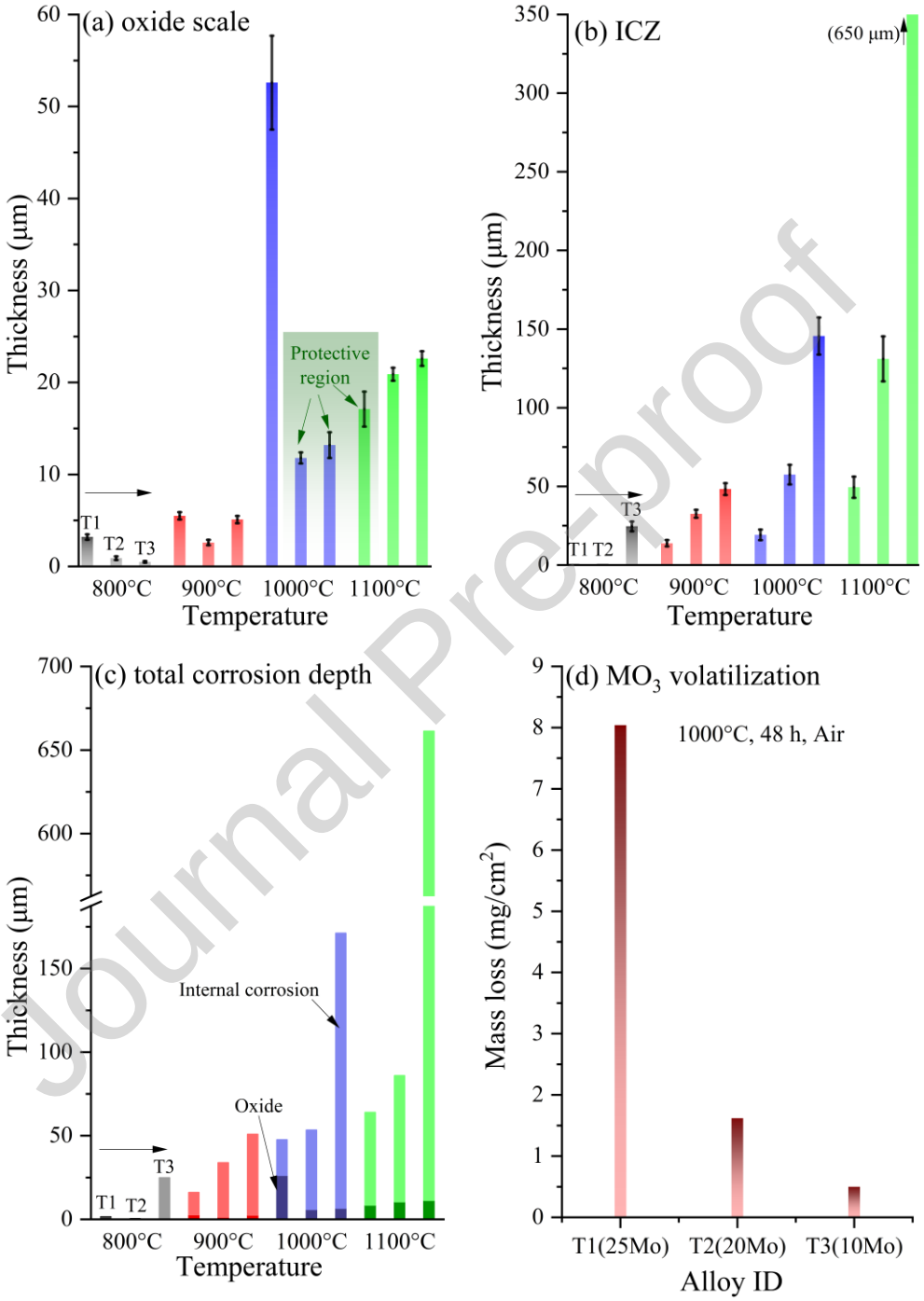

Fig. 12 Scale thickness, total metal effected (metal loss for oxide formation + average internal corrosion), and contribution of MO_3 volatilization. (a) Oxide scale thickness, (b) internal corrosion zone (ICZ) thickness, (c) total corrosion depth of the three alloys after oxidation from 800 to 1100 °C for 48 h in air, (d) estimation of MO_3 volatilization contributing to mass loss at 1000 °C based on scale thickness.

4.3. Comparison to other materials

Figure 13 compares the oxidation performance of the three alloys with TiAl-based alloys and selected RCCAs. In cases of substantial MoO_3 volatilization accompanied by mass loss, corrected mass gains based on scale thickness are used (see Table S2). In Fig. 13(a), their mass gains are quantitatively compared with TiAl4822 alloys (which have a similar Ti content) after oxidation at 800 °C and 900 °C. Notably, T1 to T3 exhibit improved oxidation resistance relative to TiAl4822 alloys with generally lower mass gains, particularly at 900 °C. Compared to most RCCAs, our alloys show evidently lower mass gains after oxidation at 1000 °C for 48 h (Fig. 13(b)), except for the equimolar TaMoCrTiAl alloy. RCCAs containing Zr, V, Hf, or W generally show poor oxidation resistance due to non-protective scale formation [3]. The considerably lower mass gains, particularly for T2 and T3, highlight their reasonable oxidation resistance up to 1000 °C. In contrast, T1 shows higher mass gain than NbMoCrTiAl and WMoCrTiAl, attributed to the global scale failure (breakaway oxidation) induced by MoO_3 volatilization associated with its high Mo content.

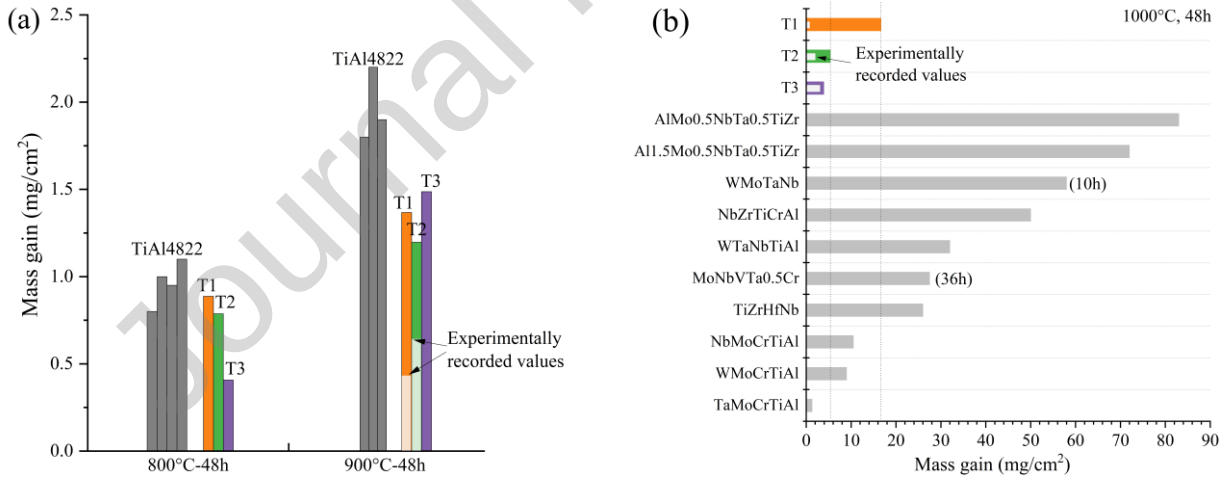

Fig. 13 Comparison of the oxidation performance of the three alloys with other materials.(a) Mass gain vs TiAl4822 alloys [30,38,56,57] *after oxidation at 800 and 900 °C. (b) Mass gain vs selected refractory high-entropy alloys after oxidation at 1000 °C* [14,58–62]. *Oxidation periods are 48 h, unless otherwise specified. Calculated (corrected) mass gains were used in cases with substantial MoO_3 volatilization and experimentally recorded values are indicated.*

Figure 14 illustrates the Arrhenius plots of the parabolic rate constants of the three Ti-rich alloys, alongside TiO_2 scale, TiAl-based alloys, and equimolar TaMoCrTiAl alloy. For conditions with considerable MoO_3 volatilization (solid star symbols; see also Table 2), similarly corrected data were used assuming overall parabolic oxidation kinetics to allow valid comparison. For the 48 h exposure, the parabolic rate constants of our alloys are approximately an order of magnitude higher than those of equimolar TaMoCrTiAl, which can be correlated to the fast growth of the TiO_2 surface layer. At lower temperatures (800 °C and 900 °C), their parabolic rate constants align with those of TiAl alloys. However, at higher temperatures, the rate constants are significantly lower than those of TiAl alloys and approach values characteristic of Cr–Ta-based complex oxides, attributed to the formation of the inner rutile-structured complex oxide layers. It should be noted that mass gain or parabolic rate constant alone are not sufficient parameters to assess the intrinsic oxidation performance of materials, especially when they undergo gas-phase oxide formation with mass loss or excessive internal corrosion of internal nitride/oxide formation or brittle oxygen-rich zone [36,54]. Instead, a more comprehensive evaluation should consider the total degradation/corrosion depth of the matrix, which includes both the thickness of the formed oxide layer and the internal corrosion zone (Fig.12).

Considering oxide scale protectiveness, MoO_3 volatilization, and internal nitridation, the maximum long-term application temperature for these alloys lies at around 900 °C. Further compositional optimization, such as slight increase of Al/Cr content or doping with Si or reactive elements [55], could enhance oxidation resistance and extend their operational temperature range.

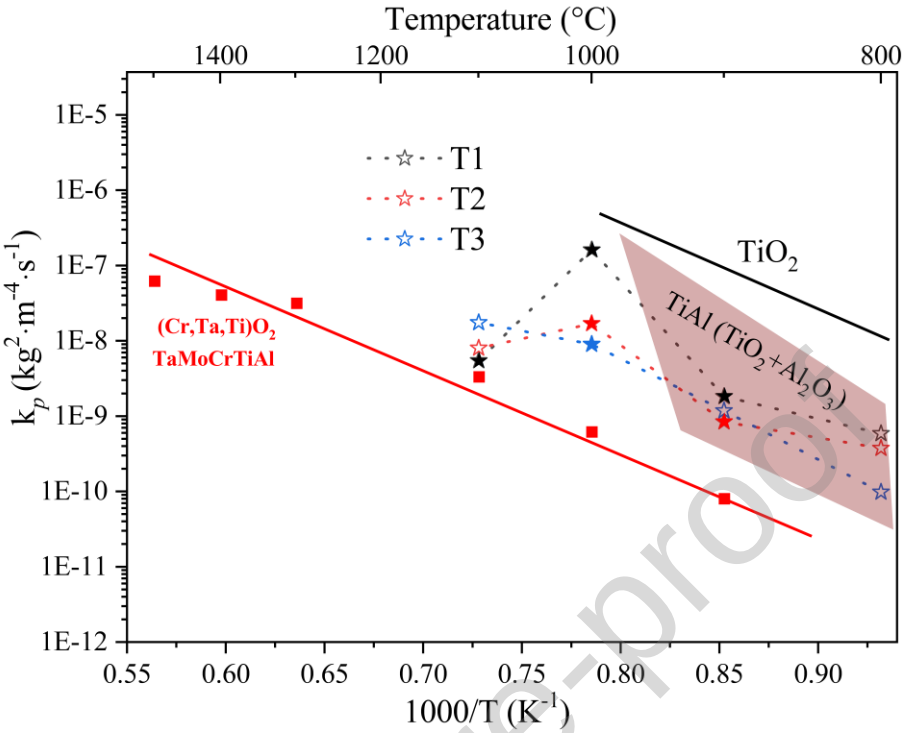

Fig. 14 Arrhenius plots of the parabolic rate constants in comparison with other materials (after [5] *and* [63]*). The solid star symbols represent the corrected parabolic rate constants after accounting for MoO_3 volatilization.*

5. Conclusions

The high-temperature oxidation behavior of three Ti-rich TiMoTaCrAl RCCAs, characterized by density of ~7.5 g/cm^3 and exhibiting room-temperature plasticity, was systematically investigated. The following conclusions can be drawn:

1) Among the three Ti-rich TiMoTaCrAl alloys, T2 (44Ti–20Mo–15Ta–15Cr–6Al) shows the best oxidation resistance, outperforming conventional TiAl-based alloys particularly above 800 °C. The thermally grown oxide scale remains protective up to 900 °C, beyond which volatilization of MoO_3 and internal nitridation limit long-term applicability. In contrast, T3 (54Ti–10Mo–15Ta–15Cr–6Al) can be excluded as a candidate due to pronounced internal nitridation across the entire investigated temperature range.
2) These Ti-rich RCCAs offer a unique combination of relatively low density (significantly lower than Ni-based superalloys but higher than TiAl), room-temperature ductility with

retained high-temperature strength, a rare combination for oxidation-resistant refractory-based alloys, making them promise for weight-critical applications in the intermediate-to-high temperature regime (700 to 900°C).

3) The oxide scale exhibits a four-sublayer structure: TiO_2, $(Cr,Al)_2O_3$, and two inner, rutile-structured complex oxide layers of $(Cr,Ti,Ta)O_2$ and $(Ti,Ta)O_2$ containing metallic Mo particles, accompanied by an internal nitridation zone. Mo particles within the inner $(Ti,Ta)O_2$ layer are progressively oxidized and volatilize through existing pores and micro-cracks. Consequently, oxide volatilization and internal nitridation cause mass change an unreliable indicator of intrinsic oxidation resistance, particularly at elevated temperatures.
4) Alloy modifications such as slightly increasing Al/Cr content or adding reactive element dopants (e.g., Hf, Y) could further enhance oxidation resistance and push the temperature limit. Future development will be directed towards achieving the most balanced property portfolio (phase stability, mechanical performance and oxidation resistance) within the 700–1000 °C range while targeting the lowest possible density.

Declaration of Competing Interest

The authors declare that they have no known competing financial interests or personal relationships that could have appeared to influence the work reported in this paper.

Acknowledgements

The authors acknowledge the financial support provided by the Deutsche Forschungsgemeinschaft (DFG, GO 2283/8-1, KA 4631/6-1, HE 1872/45-1). We acknowledge the chemical analysis by Dr. Bergfeldt at the Institute for Applied Materials (IAM-AWP).

Author Contributions

Chongchong Tang: Investigation, Formal analysis, Methodology, Data Curation, Visualization, Writing - Original Draft, Writing - Review & Editing

Amin Radi: Investigation, Writing - Review & Editing

Michael Dürrschnabel: Investigation, Writing - Review & Editing

Ute Jäntsch: Investigation, Writing - Review & Editing

Michael Klimenkov: Investigation, Writing - Review & Editing

Alexander Kauffmann: Conceptualization, Resources, Funding acquisition, Writing - Review & Editing

Martin Heilmaier: Resources, Funding acquisition, Writing - Review & Editing

Carsten Schroer: Resources, Writing - Review & Editing

Bronislava Gorr: Supervision, Conceptualization, Resources, Funding acquisition, Writing - Review & Editing

References

[1] O.N. Senkov, G.B. Wilks, D.B. Miracle, C.P. Chuang, P.K. Liaw, Refractory high-entropy alloys, Intermetallics 18 (2010) 1758–1765. https://doi.org/10.1016/j.intermet.2010.05.014.

[2] W. Xiong, A.X.Y. Guo, S. Zhan, C.T. Liu, S.C. Cao, Refractory high-entropy alloys: A focused review of preparation methods and properties, J. Mater. Sci. Technol. 142 (2023) 196–215. https://doi.org/10.1016/j.jmst.2022.08.046.

[3] B. Gorr, S. Schellert, F. Müller, H.J. Christ, A. Kauffmann, M. Heilmaier, Current Status of Research on the Oxidation Behavior of Refractory High Entropy Alloys, Adv. Eng. Mater. 23 (2021) 2001047. https://doi.org/10.1002/adem.202001047.

[4] S. Schellert, M. Weber, H.J. Christ, C. Wiktor, B. Butz, M.C. Galetz, S. Laube, A. Kauffmann, M. Heilmaier, B. Gorr, Formation of rutile (Cr,Ta,Ti)O2 oxides during oxidation of refractory high

entropy alloys in Ta-Mo-Cr-Ti-Al system, Corros. Sci. 211 (2023) 110885. https://doi.org/10.1016/j.corsci.2022.110885.

[5] B. Gorr, F. Müller, S. Schellert, H.J. Christ, H. Chen, A. Kauffmann, M. Heilmaier, A new strategy to intrinsically protect refractory metal based alloys at ultra high temperatures, Corros. Sci. 166 (2020) 108475. https://doi.org/10.1016/j.corsci.2020.108475.

[6] F. Müller, B. Gorr, H.J. Christ, H. Chen, A. Kauffmann, S. Laube, M. Heilmaier, Formation of complex intermetallic phases in novel refractory high-entropy alloys NbMoCrTiAl and TaMoCrTiAl: Thermodynamic assessment and experimental validation, J. Alloys Compd. 842 (2020) 155726. https://doi.org/10.1016/j.jallcom.2020.155726.

[7] S. Laube, A. Kauffmann, S. Schellert, S. Seils, A.S. Tirunilai, C. Greiner, Y.M. Eggeler, B. Gorr, H.J. Christ, M. Heilmaier, Formation and thermal stability of two-phase microstructures in Al-containing refractory compositionally complex alloys, Sci. Technol. Adv. Mater. 23 (2022) 692–706. https://doi.org/10.1080/14686996.2022.2132118.

[8] K. Khanchych, C. Tang, C. Schroer, B. Schäfer, J. Jung, M. Dürrschnabel, U. Jäntsch, B. Gorr, CALPHAD-Guided Prediction and Interpretation of Phase Formation in Ta–Mo–Cr–Ti–Al Refractory High-Entropy Alloys, Adv. Eng. Mater. 2500527 (2025). https://doi.org/10.1002/adem.202500527.

[9] A.E. Mann, J.W. Newkirk, Compositional Modifications to Alter and Suppress Laves Phases in AlxCrMoTayTi Alloys, Adv. Eng. Mater. 25 (2023) 1–8. https://doi.org/10.1002/adem.202201614.

[10] H. Chen, A. Kauffmann, S. Seils, T. Boll, C.H. Liebscher, I. Harding, K.S. Kumar, D.V. Szabó, S. Schlabach, S. Kauffmann-Weiss, F. Müller, B. Gorr, H.-J. Christ, M. Heilmaier, Crystallographic ordering in a series of Al-containing refractory high entropy alloys Ta-Nb-Mo-Cr-Ti-Al, Acta Mater. 176 (2019) 123–133. https://doi.org/https://doi.org/10.1016/j.actamat.2019.07.001.

[11] S. Laube, S. Schellert, A. Srinivasan Tirunilai, D. Schliephake, B. Gorr, H.J. Christ, A. Kauffmann, M. Heilmaier, Microstructure tailoring of Al-containing compositionally complex alloys by controlling the sequence of precipitation and ordering, Acta Mater. 218 (2021) 117217. https://doi.org/10.1016/j.actamat.2021.117217.

[12] S. Laube, G. Winkens, A. Kauffmann, J. Li, C. Kirchlechner, M. Heilmaier, Strength of Disordered and Ordered Al-Containing Refractory High-Entropy Alloys, Adv. Eng. Mater. 2301797 (2024) 19–21. https://doi.org/10.1002/adem.202301797.

[13] L. Yang, S. Sen, D. Schliephake, R.J. Vikram, S. Laube, A. Pramanik, A. Chauhan, S. Neumeier, M. Heilmaier, A. Kauffmann, Creep behavior of a precipitation-strengthened A2-B2 refractory high entropy alloy, Acta Mater. 288 (2025) 120827. https://doi.org/10.1016/j.actamat.2025.120827.

[14] F. Müller, B. Gorr, H.J. Christ, J. Müller, B. Butz, H. Chen, A. Kauffmann, M. Heilmaier, On the oxidation mechanism of refractory high entropy alloys, Corros. Sci. 159 (2019) 108161. https://doi.org/10.1016/j.corsci.2019.108161.

[15] T. Wang, C. Wang, J. Li, W. Wang, L. Chai, J. Luo, Oxidation resistance, corrosion behavior and grinding performance of laser-deposited TaMoCrTiAl refractory high-entropy coating, Int. J. Refract. Met. Hard Mater. 123 (2024) 106771. https://doi.org/10.1016/j.ijrmhm.2024.106771.

[16] M. Rosar, Mikrostrukturelle Charakterisierun von mehrphasigen Hochtemperaturlegierungen auf Refraktärmetallbasis, Bachelorarbeit, Karlsruhe Institute of Technology (KIT), 2021.

[17] M. Schütze, W.J. Quadakkers, Future Directions in the Field of High-Temperature Corrosion Research, Oxid. Met. 87 (2017) 681–704. https://doi.org/10.1007/s11085-017-9719-3.

[18] C. Tang, B. Schäfer, C. Schroer, B. Gorr, Improved oxidation behavior of M–20Cr–20Ta (M : Ni , Fe , Co) ternary alloys by formation of complex Cr – Ta-based oxides, Corros. Sci. 249 (2025) 112847. https://doi.org/10.1016/j.corsci.2025.112847.

[19] S. Schellert, B. Gorr, S. Laube, A. Kauffmann, M. Heilmaier, H.J. Christ, Oxidation mechanism of refractory high entropy alloys Ta-Mo-Cr-Ti-Al with varying Ta content, Corros. Sci. 192 (2021) 109861. https://doi.org/10.1016/j.corsci.2021.109861.

[20] S. Schellert, B. Gorr, H.J. Christ, C. Pritzel, S. Laube, A. Kauffmann, M. Heilmaier, The Effect of Al on the Formation of a CrTaO4 Layer in Refractory High Entropy Alloys Ta-Mo-Cr-Ti-xAl, Oxid. Met. 96 (2021) 333–345. https://doi.org/10.1007/s11085-021-10046-7.

[21] W. Ren, F. Ouyang, B. Ding, Y. Zhong, J. Yu, Z. Ren, L. Zhou, The influence of CrTaO4 layer on the oxidation behavior of a directionally-solidified nickel-based superalloy at 850–900 °C, J. Alloys Compd. 724 (2017) 565–574. https://doi.org/10.1016/j.jallcom.2017.07.066.

[22] J.W.X. Wo, M.C. Hardy, H.J. Stone, The Effect of Nb, Ta, and Ti on the Oxidation of a New Polycrystalline Ni-Based Superalloy, High Temp. Corros. Mater. 101 (2024) 485–509. https://doi.org/10.1007/s11085-023-10218-7.

[23] M. Louis Etienne, G. Stéphane, L. Guillaume, M. Hideyuki, Microstructure and oxidation

behavior of Co–Cr–Ta ternary alloys, J. Alloys Compd. 936 (2023) 167968. https://doi.org/10.1016/j.jallcom.2022.167968.

[24] O.N. Senkov, S. Gorsse, D.B. Miracle, S.I. Rao, T.M. Butler, Correlations to improve high-temperature strength and room temperature ductility of refractory complex concentrated alloys, Mater. Des. 239 (2024) 112762. https://doi.org/10.1016/j.matdes.2024.112762.

[25] O.N. Senkov, B. Crossman, S.I. Rao, J.P. Couzinie, D.B. Miracle, T.M. Butler, R. Banerjee, M. Mills, Mechanical properties of an Al10Nb20Ta15Ti30V5Zr20 A2/B2 refractory superalloy and its constituent phases, Acta Mater. 254 (2023) 119017. https://doi.org/10.1016/j.actamat.2023.119017.

[26] S. Wang, M. Wu, D. Shu, G. Zhu, D. Wang, B. Sun, Mechanical instability and tensile properties of TiZrHfNbTa high entropy alloy at cryogenic temperatures, Acta Mater. 201 (2020) 517–527. https://doi.org/10.1016/j.actamat.2020.10.044.

[27] O.N. Senkov, D.B. Miracle, K.J. Chaput, J.P. Couzinie, Development and exploration of refractory high entropy alloys - A review, J. Mater. Res. 33 (2018) 3092–3128. https://doi.org/10.1557/jmr.2018.153.

[28] S. Sheikh, M.K. Bijaksana, A. Motallebzadeh, S. Shafeie, A. Lozinko, L. Gan, T.K. Tsao, U. Klement, D. Canadinc, H. Murakami, S. Guo, Accelerated oxidation in ductile refractory high-entropy alloys, Intermetallics 97 (2018) 58–66. https://doi.org/10.1016/j.intermet.2018.04.001.

[29] O. Genc, R. Unal, Development of gamma titanium aluminide (γ-TiAl) alloys: A review, J. Alloys Compd. 929 (2022) 167262. https://doi.org/10.1016/j.jallcom.2022.167262.

[30] L. Mengis, A.S. Ulrich, P. Watermeyer, C.H. Liebscher, M.C. Galetz, Oxidation behaviour and related microstructural changes of two β0–phase containing TiAl alloys between 600 °C and 900 °C, Corros. Sci. 178 (2021) 1–10. https://doi.org/10.1016/j.corsci.2020.109085.

[31] B.A. Pint, J.R. DiStefano, I.G. Wright, Oxidation resistance: One barrier to moving beyond Ni-base superalloys, Mater. Sci. Eng. A 415 (2006) 255–263. https://doi.org/10.1016/j.msea.2005.09.091.

[32] H. Asteman, M. Spiegel, A comparison of the oxidation behaviours of Al2O3 formers and Cr2O3 formers at 700 °C - Oxide solid solutions acting as a template for nucleation, Corros. Sci. 50 (2008) 1734–1743. https://doi.org/10.1016/j.corsci.2007.12.012.

[33] H. Shi, A. Jianu, R. Fetzer, D.V. Szabó, S. Schlabach, A. Weisenburger, C. Tang, A. Heinzel, F.

Lang, G. Müller, Compatibility and microstructure evolution of Al-Cr-Fe-Ni high entropy model alloys exposed to oxygen-containing molten lead, Corros. Sci. 189 (2021) 109593. https://doi.org/10.1016/j.corsci.2021.109593.

[34] P. Zhao, H. Zhao, J. Yu, H. Zhang, H. Gao, Q. Chen, Crystal structure and properties of Al2O3-Cr2O3 solid solutions with different Cr2O3 contents, Ceram. Int. 44 (2018) 1356–1361. https://doi.org/10.1016/j.ceramint.2017.08.195.

[35] N.J. Welch, M.J. Quintana, S.J. Kuhr, T.M. Butler, P.C. Collins, Intermediate and high-temperature oxidation behavior of an equiatomic TaTiCr RCCA from 800 °C to 1400 °C, Int. J. Refract. Met. Hard Mater. 118 (2024) 106437. https://doi.org/10.1016/j.ijrmhm.2023.106437.

[36] A. Rahmel, M. Schütze, W.J. Quadakkers, Fundamentals of TiAl oxidation – A critical review, Mater. Corros. 46 (1995) 271–285. https://doi.org/10.1002/maco.19950460503.

[37] S. Becker, A. Rahmel, M. Schorr, M. Schütze, Mechanism of isothermal oxidation of the intel-metallic TiAl and of TiAl alloys, Oxid. Met. 38 (1992) 425–464. https://doi.org/10.1007/BF00665663.

[38] V.A.C. Haanappel, J.D. Sunderkötter, M.F. Stroosnijder, Isothermal and cyclic high temperature oxidation behaviour of Ti-48Al-2Mn-2Nb compared with Ti-48Al-2Cr-2Nb and Ti-48Al-2Cr, Intermetallics 7 (1999) 529–541. https://doi.org/10.1016/S0966-9795(98)00076-4.

[39] Z. Gao, R. Hu, H. Zou, M. Zhou, X. Luo, Insight into the Ta alloying effects on the oxidation behavior and mechanism of cast TiAl alloy, Mater. Des. 241 (2024) 112941. https://doi.org/10.1016/j.matdes.2024.112941.

[40] H. Yi, L. Ni, B. Yin, M. Liang, H. Yang, Y. Yang, Investigation on oxidation behavior and mechanical properties of FeCoNiNbAlCrTa high entropy alloy at 900 °C, J. Mater. Res. Technol. 33 (2024) 9405–9414. https://doi.org/10.1016/j.jmrt.2024.11.250.

[41] W.J. Nowak, B. Wierzba, J. Sieniawski, Effect of Ti and Ta on Oxidation Kinetic of Chromia Forming Ni-Base Superalloys in Ar-O2-Based Atmosphere, High Temp. Mater. Process. 37 (2018) 801–806. https://doi.org/10.1515/htmp-2017-0089.

[42] G.R. Smolik, D.A. Petti, S.T. Schuetz, Oxidation and volatilization of TZM alloy in air, J. Nucl. Mater. 283–287 (2000) 1458–1462. https://doi.org/10.1016/S0022-3115(00)00303-2.

[43] E.A. Gulbransen, K.F. Andrew, F.A. Brassart, Oxidation of Molybdenum 550° to 1700°C, J. Electrochem. Soc. 110 (1963) 952. https://doi.org/10.1149/1.2425918.

[44] P.J. Meschter, E.J. Opila, N.S. Jacobson, Water Vapor–Mediated Volatilization of High-Temperature Materials, Annu. Rev. Mater. Res. 43 (2013) 559–588. https://doi.org/10.1146/annurev-matsci-071312-121636.

[45] D.J. Young, High Temperature Oxidation and Corrosion of Metals, Elsevier, 2008. https://doi.org/10.1016/S1875-9491(08)00010-0.

[46] R. Su, H. Zhang, G. Ouyang, L. Liu, D.D. Johnson, J.H. Perepezko, Oxidation mechanism in a refractory multiple-principal-element alloy at high temperature, Acta Mater. 246 (2023) 118719. https://doi.org/10.1016/j.actamat.2023.118719.

[47] V.K. Tolpygo, D.R. Clarke, Competition Between Stress Generation and Relaxation During Oxidation of an Fe-Cr-Al-Y Alloy, Oxid. Met. 49 (1998) 187–212. https://doi.org/10.1023/A:1018828619028.

[48] C. Xu, W. Gao, Pilling-bedworth ratio for oxidation of alloys, Mater. Res. Innov. 3 (2000) 231–235. https://doi.org/10.1007/s100190050008.

[49] K. Aigner, W. Lengauer, D. Rafaja, P. Ettmayer, Lattice parameters and thermal expansion of Ti(CxN1-x), Zr(CxN1-x), Hf(CxN1-x) and TiN1-x from 298 to 1473 K as investigated by high-temperature X-ray diffraction, J. Alloys Compd. 215 (1994) 121–126. https://doi.org/10.1016/0925-8388(94)90828-1.

[50] S. Zhang, X. Wang, C. Zhang, H. Xiang, Y. Li, C. Fang, M. Li, H. Wang, Y. Zhou, Microstructure, elastic/mechanical and thermal properties of CrTaO4: A new thermal barrier material?, J. Adv. Ceram. 13 (2024) 373–387. https://doi.org/10.26599/jac.2024.9220862.

[51] J.J. Barnes, J.G. Goedjen, D.A. Shores, A Model for stress generation and relief in Oxide - Metal systems during a temperature change, Oxid. Met. 32 (1989) 449–469. https://doi.org/10.1007/BF00665449.

[52] Y. Kang, M.K. Paek, I.H. Jung, Critical thermodynamic assessment of Mo–C, Mo–N, and Mo–C–N systems, and its application to Mo carbo-nitride synthesis, J. Mater. Res. 37 (2022) 2979–2995. https://doi.org/10.1557/s43578-022-00702-2.

[53] F. Hinrichs, A. Kauffmann, A.S. Tirunilai, D. Schliephake, B. Beichert, G. Winkens, K. Beck, A.S. Ulrich, M.C. Galetz, Z. Long, H. Thota, Y. Eggeler, A. Pundt, M. Heilmaier, A novel nitridation- and pesting-resistant Cr-Si-Mo alloy, Corros. Sci. 207 (2022) 110566. https://doi.org/10.1016/j.corsci.2022.110566.

[54] R. Pillai, A. Chyrkin, W.J. Quadakkers, Modeling in High Temperature Corrosion: A Review and Outlook, Springer US, 2021. https://doi.org/10.1007/s11085-021-10033-y.

[55] Y. Du, D. Ding, L. Lai, S. Xiao, N. Guo, B. Song, S. Guo, Effect of Y on the high-temperature oxidation behavior of CrMoTaTi refractory high entropy alloy, Int. J. Refract. Met. Hard Mater. 103 (2022) 105755. https://doi.org/10.1016/j.ijrmhm.2021.105755.

[56] S. Tian, T. Zhang, S. Zeng, Y. Zhang, D. Song, Y. Chen, Q. Kang, H. Jiang, Cyclic Oxidation Kinetics and Thermal Stress Evolution of TiAl Alloys at High Temperature, Metals (Basel). 14 (2024). https://doi.org/10.3390/met14010028.

[57] W. Zhu, Y.Y. He, X. Cui, Y.Y. He, B. Li, C. Zhang, Microstructure refinement and oxidation behavior improvement in Mo modified TiAl4822 alloy prepared by vacuum sintering, Vacuum 202 (2022). https://doi.org/10.1016/j.vacuum.2022.111122.

[58] Y. Yan, K.A. McGarrity, D.J. Delia, C. Fekety, K. Wang, The oxidation-resistance mechanism of WTaNbTiAl refractory high entropy alloy, Corros. Sci. 204 (2022) 110377. https://doi.org/10.1016/j.corsci.2022.110377.

[59] M. Guo, L. Xu, Y. Zhao, S. Deng, Z. Li, S. Wei, High temperature oxidation behavior and mechanism of MoNbVTa0.5Crx refractory high entropy alloys, Corros. Sci. 245 (2025). https://doi.org/10.1016/j.corsci.2024.112672.

[60] S. Lu, X. Li, X. Liang, W. Yang, J. Chen, Effect of V and Ti on the oxidation resistance of wmotanb refractory high-entropy alloy at high temperatures, Metals (Basel). 12 (2022). https://doi.org/10.3390/met12010041.

[61] H. Ke, A. Wang, Y. Qiao, Y. Xue, Comparative investigation of high temperature oxidation behavior of single-phase equi-atomic Ti-Zr-Hf-Nb alloys : From binary to quaternary, J. Alloys Compd. 1039 (2025) 182979. https://doi.org/10.1016/j.jallcom.2025.182979.

[62] M. Mokhtare, M. Zohrevand, A. Momeni, S. Sadeghpour, A. Amanov, Effects of Re addition and initial microstructure on high-temperature oxidation of AlMo0.5NbTa0.5TiZr refractory high entropy alloy, Int. J. Refract. Met. Hard Mater. 133 (2025) 107319. https://doi.org/10.1016/j.ijrmhm.2025.107319.

[63] X. Xu, H. Liang, H. Ding, K.P. Davidson, R. V. Ramanujan, R. Chen, J. Guo, H. Fu, Oxidation behavior and mechanical properties of a directionally solidified high Nb TiAl based alloy between 800 °C and 900 °C, Intermetallics 176 (2025) 108538.

https://doi.org/10.1016/j.intermet.2024.108538.